

Water Resources Research®








RESEARCH ARTICLE

10.1029/2025WR040146

A Dynamic Network Model for Forced Imbibition Considering Competition Between Main-Meniscus Flow and Corner Flow

Key Points:

- A theoretical model to predict transition from main-meniscus flow to corner flow is derived by interplay of capillary and viscous forces
- A dynamic network model incorporating local competition between main-meniscus flow and corner flow is established
- Lenormand's phase diagram is extended to strong imbibition with corner flow event in heterogeneous porous media

Wenbo Gong^{1,2,3} , Wenhai Lei⁴ , Tian Tian⁵, Jiangtao Zheng⁵ , Yang Liu², Yuedi Wang², Yang Ju⁵ , and Moran Wang² 

¹Hainan Institute, China University of Petroleum (Beijing), Hainan, China, ²Department of Engineering Mechanics, Tsinghua University, Beijing, China, ³College of Safety and Ocean Engineering, China University of Petroleum, Beijing, China, ⁴Department of Engineering Mechanics, KTH Royal Institute of Technology, Stockholm, Sweden, ⁵State Key Laboratory for Fine Exploration and Intelligent Development of Coal Resources, China University of Mining and Technology-Beijing, Beijing, China

Correspondence to:

M. Wang,
mrwang@tsinghua.edu.cn

Citation:

Gong, W., Lei, W., Tian, T., Zheng, J., Liu, Y., Wang, Y., et al. (2025). A dynamic network model for forced imbibition considering competition between main-meniscus flow and corner flow. *Water Resources Research*, 61, e2025WR040146. <https://doi.org/10.1029/2025WR040146>

Received 28 FEB 2025
Accepted 11 JUN 2025

Author Contributions:

Conceptualization: Moran Wang
Data curation: Wenhai Lei, Jiangtao Zheng, Yang Liu
Investigation: Wenbo Gong, Jiangtao Zheng, Yuedi Wang
Methodology: Wenbo Gong
Project administration: Moran Wang
Resources: Yuedi Wang, Yang Ju
Supervision: Moran Wang
Validation: Wenhai Lei, Tian Tian, Yang Liu
Writing – original draft: Wenbo Gong
Writing – review & editing: Wenhai Lei, Tian Tian, Jiangtao Zheng, Yang Ju, Moran Wang

Abstract The pore-scale interfacial dynamics including main-meniscus flow and corner flow usually occurs in heterogeneous porous media and significantly affects the macroscopic multiphase flow process. Numerical research on the competition between main-meniscus flow and corner flow remains challenging due to the ambiguity in pore-scale interfacial dynamics and the complexity of upscaling these processes to porous media, given the substantial spatial and temporal scale differences. In this study, we proposed a critical capillary number (Ca_c) by considering the interplay of local capillary and viscous forces, which predicts transition from main-meniscus flow-dominated processes into corner flow-dominated processes during the strong imbibition. The Ca_c criterion was integrated into a dynamic network model to translate pore-scale interfacial dynamics into multiphase flow patterns in porous media. The forced imbibition in heterogeneous porous media under different Ca were simulated and compared to microfluidic experimental data. The comparison indicates that the dynamic competition between main-meniscus flow and corner flow has a vital impact on displacement behaviors predicted by pore-scale modeling, and our dynamic network model accurately captures the interfacial dynamics observed in microfluidic experiments. Moreover, the impact of interfacial dynamics on macroscopic multiphase flow pattern and displacement efficiency in heterogeneous porous media were addressed during strong imbibition under various viscosity ratios and capillary numbers. The phase diagram manifests a monotonic effect of viscosity ratio on displacement efficiency at high Ca due to the dominance of viscous fingering. A non-monotonic effect of viscosity ratio is revealed at low Ca , which is ascribed into competition between corner flow and main-meniscus flow. This study highlights the gap in the existing models of interfacial dynamics at pore scale, and provide an effective upscaling approach to investigate the multiphase flow in porous media.

1. Introduction

Multiphase flow in porous media plays a crucial role in both natural processes and engineering applications, such as oil and gas recovery (Celia et al., 1995), geological sequestration of carbon dioxide (Chen et al., 2019), and transport of interstitial fluids in the human brain (Goirand et al., 2021). This process is inherently constrained by porous media and exhibits diverse interfacial dynamics at the pore scale, including fingering invasion, snap-off event, Haines jump, cooperative pore filling events, and ganglion remobilization (Armstrong & Berg, 2013; Armstrong et al., 2012; Berg et al., 2013; Bultreys et al., 2024). Pore-scale interfacial dynamics greatly affect macroscopic multiphase flow behaviors in porous media. The Lenormand's phase diagram characterizes the fluid-fluid displacement in porous media using two dimensionless parameters (Lenormand et al., 1988), the capillary number Ca ($Ca = \mu_{in}u/\sigma$) and viscosity ratio M ($M = \mu_{in}/\mu_{de}$); where μ_{in} and μ_{de} are the dynamic viscosity of invading and defending fluid, u is the characteristic velocity of invading fluid, and σ is the interfacial tension. At low Ca , the invasion pattern into pores is predominantly controlled by capillary forces, leading to the capillary fingering pattern. In contrast, at high Ca and low M , the viscous forces dominate, resulting in a viscous fingering pattern. Research on interfacial patterns has primarily focused on the main-meniscus flow, where the defending fluid is displaced completely in local pore structure.

Numerous studies have highlighted the significance of ramified interfacial displacement (Cha et al., 2021; Singh et al., 2017, 2022), which go beyond the scope of Lenormand's diagram. A typical example is corner flow, where

© 2025. The Author(s).

This is an open access article under the terms of the [Creative Commons Attribution License](https://creativecommons.org/licenses/by/4.0/), which permits use, distribution and reproduction in any medium, provided the original work is properly cited.

the wetting fluid moves along the angular edges or corners of a pore structure, bypassing the bulk region of the pore (Lenormand et al., 1983). Corner flow generally occurs during imbibition, in which capillary forces drive the wetting fluid, playing a critical role in maintaining continuity during capillary-driven processes. Specifically, the wetting fluid in the corner layers can expand until it reaches a state of pressure non-equilibrium, leading to spontaneous filling at the pore throat and the disconnection of the nonwetting fluid. This process, known as the snap-off event, often traps nonwetting fluid within the pore body, surrounded by the wetting fluid. The displacement or trapping of the nonwetting fluid is of particular importance: maximum trapping efficiency is desired for CO₂ storage, while reduced trapping is beneficial for enhanced displacement efficiency. In contrast to the interfacial patterns observed during drainage, the imbibition process is primarily driven by two key mechanisms at the pore scale: main-meniscus flow and corner flow (Joekar-Niasar & Hassanizadeh, 2012). These mechanisms significantly influence macroscopic flow patterns and displacement efficiency. Understanding the dynamic competition between main-meniscus and corner flow remains challenging, particularly in heterogeneous porous media, where capillary and viscous forces interact in intricate ways. Upscaling these dynamic interfacial phenomena at pore scale to macroscopic flow simulations is essential for a wide range of applications (Ebadi et al., 2024), such as underground hydrogen storage, geological carbon sequestration, and hydrocarbon recovery. Bridging the gap between pore-scale behaviors and macroscopic processes thus requires the development of a robust theoretical framework.

Despite considerable advancements in both experimental and numerical studies, current approaches still face several limitations. Advanced microfluidic model and computed-tomography scanning experiments have visualized institutively on multiphase flow in porous media and provided insights into interfacial dynamics (Anbari et al., 2018; Hu et al., 2019; Ju et al., 2022; Lan et al., 2020; Lei et al., 2022; Li, Yang, Pahlavan, et al., 2024; Sinton, 2014). However, these studies often neglect the dynamic competition between main-meniscus flow and corner flow, focusing primarily on the former. Furthermore, experimental observations are limited by trade-offs between imaging resolution and field of view, which constrain the simultaneous capture of pore-scale dynamics and macroscopic displacement processes (Lei et al., 2022). Numerical methods, including direct numerical simulations like the level-set method, volume-of-fluid method, phase-field method, and multiphase models of lattice Boltzmann method (Li, Yang, Huang, et al., 2024; Liu et al., 2016; Raeini et al., 2012; Xie et al., 2018; Zhao et al., 2019), offer detailed tracking of fluid interfaces but are computationally expensive, restricting their application to small-scale domains. For instance, as noted in reference (Chen et al., 2019), an LBM simulation of liquid CO₂ displacing water in a Bentheimer sandstone with a physical size of 2.29 × 2.29 × 2.75 mm and a domain size of 720 × 720 × 864 took 55 hr to complete the injection of one pore volume using 20 NVIDIA V100 GPUs. Given these challenges, the dynamic network model has emerged as a powerful alternative, offering a unique balance between computational efficiency and accuracy for simulating multiphase flow in porous media (Joekar-Niasar & Hassanizadeh, 2012). The simplification of porous structure significantly enhances computation efficiency (An et al., 2020; Liu et al., 2022; Raeini et al., 2017), while a reliable understanding of pore-scale interfacial dynamics is required for accurate predictions on multiphase flow in porous media.

In natural porous media, interfacial patterns such as main-meniscus flow and corner flow are commonly observed (Geistlinger & Zulficar, 2020). The transition from corner flow along angular pore spaces to main-meniscus flow—driven by the coalescence of corner flows and commonly referred to as a snap-off event—has been extensively studied using pore-scale models (Lenormand et al., 1983; Zheng et al., 2024). However, in these models, the interfacial dynamics governing the opposite transition from main-meniscus flow to corner flow remain unclear, hindering the further development of dynamic network models. The pore-scale interfacial model proposed by Cieplak and Robbins (1988) used three types of interfacial instabilities (burst, touch, and overlap) to shape the displacement process. Subsequent studies extended this framework by incorporating viscous and wettability effects (Holtzman & Segre, 2015; Primkulov et al., 2021) and applying it to more complex geometries, including irregular porous structures (Wang et al., 2022). However, while these extensions have broadened the applicability of the model, the dynamic competition between main-meniscus flow and corner flow remains absent in the context of heterogeneous porous media. Additionally, experimental validation of this interplay in multiphase flow through heterogeneous porous structures is still lacking. The heterogeneity and anisotropy of natural porous media introduce additional complexity to interfacial dynamics during multiphase flow (Ju et al., 2020; Lei, Gong, & Wang, 2023; Singh et al., 2022; Zheng et al., 2021), leaving the onset conditions less clearly understood. For spontaneous imbibition process dominated by capillary force, the onset of corner flow can be predicted by balancing the capillary force in neighboring pores (Qin and van Brummelen, 2019). Under general multiphase

flow conditions where viscous force cannot be ignored, the corner flow at pore scale results from the competition between viscous force and capillary force within the local pore structure (Mansouri-Boroujeni et al., 2023). Refined network models have represented corner flow dynamics by decomposing a pore body into several interacting sub-pore networks (Zhao et al., 2022). In these models, main-meniscus flow and corner film flow are assumed to occur simultaneously within a pore, with the central subcapillary representing main-meniscus flow and the remaining subcapillaries representing corner film flow. However, this refinement increases computational complexity, and accurate pore-scale predictions of main-meniscus and corner flow remain lacking, particularly for fluids with differing viscosity ratios. These viscosity differences are critical in determining viscous resistance during multiphase flow (Gong et al., 2023; Shams et al., 2018; Xie et al., 2017; Zhao et al., 2022). Although prior studies have explored the competition between viscous and capillary forces, they often fail to capture transitions between main-meniscus flow and corner flow under varying viscosity ratios and flow regimes. This gap highlights the need for an integrated model that accurately represents the interplay between capillary and viscous forces to predict flow transitions and their macroscopic consequences.

In this study, the dynamic competition between main-meniscus flow and corner flow is predicted using a critical capillary number that considers the interplay of capillary and viscous forces within a local pore structure. The critical capillary number will be derived and extended to a general context by accounting for the viscous coupling effects of multiphase fluids across various viscosity ratios. Incorporating the critical capillary number, a dynamic network model will be developed to scale up the main-meniscus flow, corner flow and their dynamic competition to the level of multiphase flow in porous media. The proposed model will be validated by comparing interfacial patterns in porous media with microfluidic experimental results, and by comparing interfacial evolution in a regular tube with theoretical analysis. Additionally, forced imbibition in porous media under different capillary numbers and viscosity ratios will be simulated using the proposed model, enabling us to revisit the impact of pore-scale interfacial dynamics on multiphase displacement phenomena considering local interplay of capillary and viscous forces.

2. Numerical Model

2.1. The Basic Equations in Dynamic Network Model

The dynamic network model (DNM) consists of two main components: network extraction and pore-scale flow modeling. In network extraction, the complex pore space in porous media is simplified into a network of pores and throats (Liu et al., 2022), significantly reducing the number of computational elements required for pore-scale flow modeling. The pore-scale modeling emphasizes the primary flow dynamics averaged within each pore and throat, and is employed to examine the interaction between viscous and capillary forces during multiphase displacement (Koplik & Lasseter, 1985).

This study employs the two-pressure algorithm to describe the evolution of multiphase flow and pressure field in the pore-scale modeling, where each fluid phase in a pore body is assigned its own pressure (Joekar-Niasar & Hassanizadeh, 2012). The pressure difference between neighboring pore bodies drives the fluid flow through the connecting pore-throat channels. The extracted network consists of pore bodies, which represent void volumes, and pore throats, which account for hydraulic resistance. The multiphase fluids in the modeling are assumed to be incompressible, immiscible, and isothermal. The volumetric flow rate of each fluid through a pore-throat channel is calculated using Hagen-Poiseuille equation, and the total volumetric rate in each pore body is governed by the principle of volumetric conservation (Qin and van Brummelen, 2019):

$$Q_{ij,\alpha} = -K_{ij,\alpha}(P_{i,\alpha} - P_{j,\alpha}) \quad (1)$$

$$\sum_{j=1}^{N_i} (Q_{ij,w} + Q_{ij,n}) = 0 \quad (2)$$

where $P_{i,\alpha}$ denotes the fluid pressure in pore body i ($\alpha = w, n$ for the wetting and nonwetting phases, respectively). $Q_{ij,\alpha}$ represents the fluid flux through the pore throat ij connecting pore body i and pore body j . N_i indicates the coordinate number of pore body i (the number of throats connecting to pore body i). The hydraulic conductance of each fluid $K_{ij,\alpha}$ is a function of pore geometry and fluid saturation. When the pore throat is fully occupied by the fluid, the corresponding hydraulic conductance is (Patzek, 2001):

$$K_{ij,\alpha} = \frac{\chi G_{ij} A_{ij}^2}{\mu_{\alpha} l_{ij}} \quad (3)$$

where χ is the hydraulic conductance coefficient and the corresponding values in circular, square, and triangular cross-section are 0.5, 0.5623, and 0.6, respectively (Patzek, 2001). The shape factor is defined as $G_{ij} = A_{ij}/P_{ij}^2$ (A_{ij} and P_{ij} are the area and perimeter of the cross-section in pore throat ij) (Patzek, 2001). l_{ij} is the length of pore throat ij . μ_{α} is the dynamic viscosity of fluid α .

During the multiphase flow in a network, the variation of fluid saturation in each pore body is determined by total flux of each fluid through the connected pore throats:

$$V_i \frac{\Delta S_{i,\alpha}}{\Delta t} + \sum_{j=1}^{N_i} Q_{ij,\alpha} = 0 \quad (4)$$

where $\Delta S_{i,\alpha}$ is the saturation of fluid α during time interval Δt in the pore body i with pore volume V_i . In this study, it is assumed that the local capillary pressure is a function of wetting phase saturation only and is equal to the pressure difference in pore body i (Thompson, 2002):

$$P_{i,c}(S_{i,w}) = P_{i,n} - P_{i,w} \quad (5)$$

Following the derivation of $P_{i,c}(S_{i,w})$ for a cubic pore body with inscribed pore radius R_i in Joekar-Niasar et al.'s work (Joekar-Niasar, Hassanizadeh, & Dahle, 2010), the relationship of fluid saturation with local capillary pressure is determined as:

$$P_{i,c} = \frac{2\sigma}{R_i(1 - \exp(-6.83S_{i,w}))} \quad (6)$$

where σ is interface tension of the immiscible fluids. Two interfacial patterns, the main-meniscus flow and corner flow, are considered in dynamic network model. Corner flow can occur in a throat when the geometric condition $\theta + \beta < \pi/2$ is satisfied (Qin and van Brummelen, 2019), where θ is the contact angle on the wall and β is the half-angle of the square cross-section ($\beta = 45^\circ$). This condition ensures that capillary forces can drive the wetting phase into the corner regions under positive capillary pressure. However, satisfying this geometric condition alone does not necessarily lead to corner flow; a dynamic criterion by balancing local viscous and capillary forces should be considered to predict the onset of corner flow (Lei, Lu, et al., 2023). In this study, we incorporate both geometric and dynamic criteria to determine the onset of corner flow, ensuring a more comprehensive description of pore-scale displacement mechanisms. Besides, the capillary pressure $P_{ij,c}$ in a throat should be low enough to allow the coalescence of corner flow and results in a snap-off event (Lenormand et al., 1983):

$$P_{ij,c} \leq \frac{\sigma}{r_{ij}} (\cos \theta - \sin \theta) \quad (7)$$

where r_{ij} is the inscribed radius of a pore throat connecting to pore body i and pore body j .

During pore-scale flow modeling, a velocity boundary condition is applied at the inlet of the porous structure, while a pressure boundary is set at the outlet. Additionally, the wetting fluid saturation should be constrained, with $S_{\text{inlet},w} = 1$ at the inlet and $S_{\text{outlet},w} = S_{\text{outlet}-1,w}$ at the outlet, where $S_{\text{outlet}-1,w}$ represents the wetting fluid saturation in the pores adjacent to the outlet boundary pores. This condition ensures a zero capillary pressure gradient at the outlet (Chen et al., 2020), allowing the flow in the outlet pores to develop fully and preventing artificial boundary effects. Initially, the porous structure is occupied by the nonwetting fluid ($S_w = 0$) and no pressure difference is applied ($P_n = 0$). The wetting fluid is injected into the porous structure at a constant flux rate $Q_{\text{inlet},w}$. To simulate multiphase flow within a network, Equations 2 and 4 are solved simultaneously using a fully implicit scheme, with automatic differentiation (AD) employed to compute the partial derivatives in the computation (Bao, 2017). Unlike numerical differentiation, AD provides exact derivatives by systematically

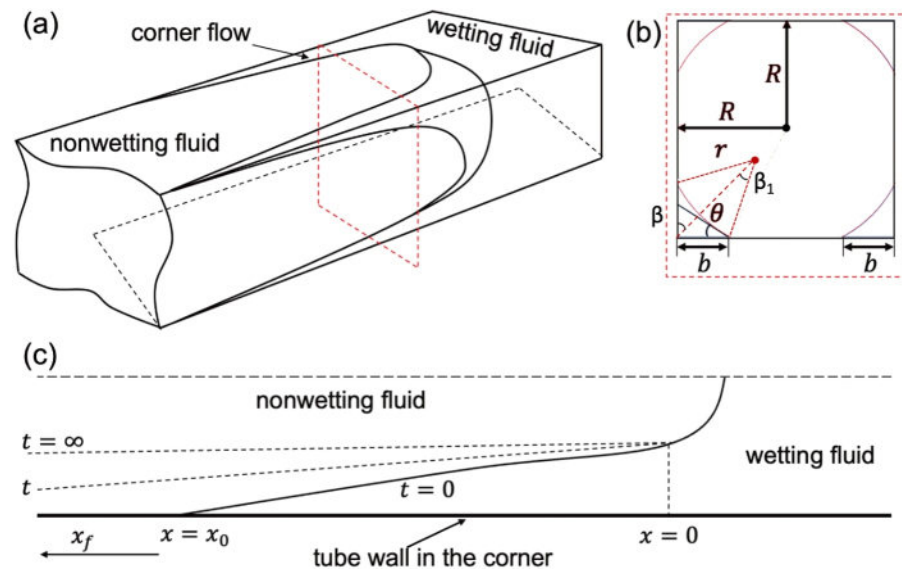


Figure 1. The sketch of corner flow during imbibition in a square tube, which is adapted from Dong and Chatzis's work (1995). (a) The situation of wetting fluid along the corners, (b) the multiphase fluid distribution in a cross-section (the red solid curve represents the multiphase interface), and (c) the spreading of corner flow during imbibition.

applying the chain rule to elementary operations, ensuring high accuracy and computational efficiency. We adopt a reverse-mode AD approach, which is particularly effective for solving large nonlinear systems, as it computes gradients efficiently regardless of the number of variables.

2.2. The Improved Dynamic Network Model

2.2.1. Theoretical Prediction on the Onset of Corner Flow in a Single Tube

The wetting fluid invades the pore space driven by the local capillary and viscous forces, and their dynamic competition results in different interfacial patterns including corner flow and main-meniscus flow. Their competition can be reflected by balancing the volumetric flow rate of fluid along the bulk and angular space within a single tube. It is worth noting that the theoretical analysis is based on the square tube with perfecting wetting condition. The multiphase flux in an angular tube is determined by the product of pressure difference and hydraulic conductance of each fluid. However, the fluid flow resistance proposed by Ransohoff and Radke (1988) is discontinuous and only applicable to multiphase fluids with specific viscosity ratios. Since multiphase flow resistance is not expressed as a function of viscosity ratio, extending the formulation of critical capillary number to general conditions with continuous viscosity variation is not feasible. Our previous work introduced a mathematical model for multiphase flow resistance with viscous coupling effect under the interfacial pattern of corner flow, as a function of viscosity ratio (Gong et al., 2023). In this subsection, we present a general framework to predict the competition between main-meniscus flow and corner flow, incorporating the hydraulic resistance model of multiphase fluids with viscous coupling effect. The governing equation for fluid flux in a square tube during the transition from main-meniscus flow to corner flow is:

$$\frac{\partial q_w}{\partial x} = -\frac{\partial A_w}{\partial t} \quad (8)$$

where q_w and A_w represent the volumetric flow rate and the area occupied by the wetting fluid at a given cross-section with area A in location x and at time t . The distribution of multiphase fluids is presented in Figure 1a. Employing Hagen-Poiseuille equation to describe fluid flow in a square tube, the volumetric flow rate can be described as:

$$q_w = -g_w \frac{\partial P_w}{\partial x} \quad (9)$$

where g_w is the hydraulic conductance of wetting fluid in the tube, and P_w is the wetting-fluid pressure. During the transition from main-meniscus flow to corner flow, the wetting fluid invades the angular spaces, while the nonwetting fluid either moves slowly or remains immobile. Therefore, the corner flow of wetting fluid is primarily driven by the local capillary pressure P_c :

$$q_w = g_w \frac{\partial P_c}{\partial x} \quad (10)$$

In corner flow, the fluid morphology exhibits a very large curvature radius in the plane parallel to the capillary tube (as shown in Figure 1b). The capillary pressure is calculated as $P_c = \sigma/r$, where r is the curvature radius of meniscus in a cross-section perpendicular to the tube axis, and the half value of central angle for this curvature is $\beta_1 = \frac{\pi}{2} - \theta - \beta$. A mathematical model accounts for the effect of viscosity ratio ($\hat{\mu} = -\log \frac{\mu_w}{\mu_n}$), contact angle (θ), and the film width (b) in the cross-section (Gong et al., 2023):

$$g_w = 2 \hat{g}_w \frac{b^4}{\mu_w} (\eta(b, \theta, \hat{\mu}) + 1) \quad (11)$$

where \hat{g}_w is the dimensionless conductance of wetting fluid ignoring the viscous coupling effect, which could be specified in the square tube (the half angle in the cross-section $\beta = 45^\circ$) with perfect wetting condition ($\theta = 0^\circ$) (Patzek, 2001):

$$\begin{aligned} \tilde{A}^w &= \left[\frac{\sin \beta}{\cos(\theta + \beta)} \right]^2 \left[\frac{\cos \theta \cos(\theta + \beta)}{\sin \beta} + \theta + \beta - \frac{\pi}{2} \right] = 1 - \frac{\pi}{4} \\ \tilde{G}^w &= \frac{\tilde{A}^w}{4 \left[1 - (\theta + \beta - \frac{\pi}{2}) \sin \beta / \cos(\theta + \beta) \right]^2} = 0.0168 \\ \hat{g}_w &= \exp \left[\frac{-15.2(\tilde{G}^w)^2 + 7.63\tilde{G}^w - 0.535 + 0.02 \sin(\beta - \frac{\pi}{6})}{(1/4\pi - \tilde{G}^w)^{7/8} \sqrt{\cos(\beta - \pi/6)}} + 2 \ln \tilde{A}^w \right] = 4.41 \times 10^{-4} \end{aligned}$$

The effect of viscous coupling with viscosity ratio is described as:

$$\eta = \frac{(60 \cos(\theta + \beta) / \sin \beta + 14)(b/R)^{-1/3}}{(5 \cos(\theta + \beta) / \sin \beta + 1.5) e^{b/(2R)} + e^{2.5\hat{\mu}}} = \frac{74(b/R)^{-1/3}}{6.5 e^{b/(2R)} + e^{2.5\hat{\mu}}} \quad (12)$$

where R is the inscribed radius of the tube, and the film width b presents the distance from meniscus apex along the wall to three-phase contact point in the cross-section, depends on the multiphase interface curvature (r), and can be expressed as $b = \max(0, r \cos(\theta + \beta) / \sin \beta) = r$ (Qin and van Brummelen, 2019), as illustrated in Figure 1b. The film length b under a perfectly wetting condition ranges from 0 to R , thereby the term $6.5 e^{b/(2R)}$ varies from 6.5 to 10.7 and could be averaged as 8.6. To simplify Equation 12, viscous coupling coefficient can be described as:

$$\eta = \frac{74(r/R)^{-1/3}}{8.6 + e^{2.5\hat{\mu}}} \quad (13)$$

The occupied area of wetting fluid in the cross-section is determined by the contact angle and the film width (Patzek, 2001; Qin and van Brummelen, 2019):

$$A_w = 4 \left(\frac{\cos \theta \cos(\theta + \beta)}{\sin \beta} + \theta + \beta - \frac{\pi}{2} \right) r^2 = Cr^2 \quad (14)$$

where the parameter C is defined as $C = 4\left(\frac{\cos \theta \cos(\theta + \beta)}{\sin \beta} + \theta + \beta - \frac{\pi}{2}\right)$. The volumetric rate of wetting fluid along the corner can be derived by combining Equations 10–14,

$$q_w = -\frac{\hat{g}_w \sigma}{\mu_w C^{3/2}} \left(\frac{74R^{1/3} C^{1/6} A_w^{1/3}}{8.6 + e^{2.56\hat{q}}} + A_w^{1/2} \right) \frac{\partial A_w}{\partial x} \quad (15)$$

When the wetting fluid in a main-meniscus flow pattern starts to invade the downstream pore space, the multiphase flow state at that moment is defined as the initial state. At this stage, the fluid interface contacts the solid wall in the cross-section normal to the tube axis. The area occupied by the wetting fluid, denoted as A_w , is assumed to be CR^2 . This initial state serves as a reference point for predicting the subsequent competition between main-meniscus flow and corner flow. A dimensionless saturation of corner flow is defined as $S = A_w/CR^2$. Substituting Equation 15 into Equation 8 and replacing the wetting fluid area A_w with the dimensionless saturation S in Equation 15 yield:

$$\frac{\partial}{\partial x} \left(\frac{\hat{g}_w \sigma R}{\mu_w C} \left(\frac{74S^{1/3}}{8.6 + e^{2.56\hat{q}}} + S^{1/2} \right) \frac{\partial S}{\partial x} \right) = \frac{\partial S}{\partial t} \quad (16)$$

It's challenging to solve the nonlinear diffusion equation with the polynomial function, the variational method (Dong & Chatzis, 1995) could be practicable to provide an expression of saturation distribution in the corner by revising the polynomial function of dimensionless saturation as its power function, $\frac{74S^{1/3}}{8.6 + e^{2.56\hat{q}}} + S^{1/2} = m_1 S^{m_2}$, where the coefficients m and n are determined by the fitting curves, $m_1 = m_0 + e^{-0.03m_0}$, $m_2 = 1/3 + e^{-m_0}/6$, and $m_0 = \frac{74}{8.6 + e^{2.56\hat{q}}}$. As shown in Figure C1 from Appendix C, the impact of the viscous ratio on the coefficients is verified and the averaged relative error is 3.75%. The governing equation for the interfacial dynamics with viscous coupling effect can be described as:

$$\frac{\partial S}{\partial t} = B \frac{\partial}{\partial x} \left(S^n \frac{\partial S}{\partial x} \right) \quad (17)$$

where $B = \hat{g}_w \frac{\sigma R}{\mu_w C} m_1$. The classical solution of this nonlinear diffusion equation for water-gas system with $n = 1/2$ were derived using variational methods with a constant pressure boundary condition (Dong & Chatzis, 1995). Similarly, the exact solution of Equation 17 of the corner flow development (illustrated in Figure 1c) could be given:

$$S = S_0 \left(1 - \frac{a_0 x}{x_f} + (a_0 - 1) \left(\frac{x}{x_f} \right)^2 \right)^{1/n} \quad (18)$$

where the initial value of the occupied area ratio $S_0 = 1$, and a_0 is a parameter introduced by the trial function. The front of spreading fluid moves according to:

$$x_f = x_0(1 + 2\nu t)^{1/2} \quad (19)$$

where the time constant ν is related to the initial shape of the liquid meniscus. The initial location of the main-meniscus x_0 is

$$x_0 = \left(\frac{K_0 B S_0^n}{n\nu} \right)^{1/2} \quad (20)$$

where the parameter K_0 is calculated using a variational method by minimizing the difference between the exact and approximate solution. With the approximation of large time ($2\nu t \gg 1$), substitution of Equation 20 into Equation 19 gives:

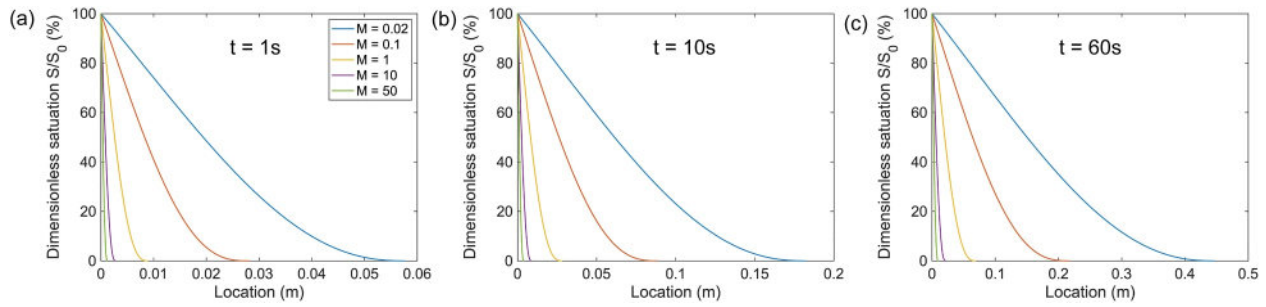


Figure 2. The dimensionless saturation distribution for the wetting fluid along the angular corner in a square cross-section with side length of 500 μm at different times: (a) $t = 1\text{s}$, (b) $t = 10\text{s}$, and (c) $t = 60\text{s}$. The viscosity of nonwetting fluid is 1 $\text{mPa} \cdot \text{s}$, and viscosity ratio $M = 0.02, 0.1, 1, 10, 50$. The interfacial tension and contact angle of multiphase fluids are 72 mN/s and 0° .

$$x_f = \left(\frac{2K_0 B S_0^n t}{n} \right)^{1/2} \quad (21)$$

The advancement of wetting fluid along the corners obeys Equation 21, leading to a temporary variation in fluid saturation within the cross-section, as predicted by Equation 18. The impact of fluid viscosity ratio on corner flow is illustrated in a square tube with side length of 500 μm , as shown in Figure 2. The viscosity of nonwetting fluid is 1 $\text{mPa} \cdot \text{s}$ and the viscosity ratios ($M = \mu_w/\mu_n$) vary from 0.02 to 50. The interfacial tension is chosen from water-gas system ($\sigma = 72 \text{ mN/s}$) with a fixed contact angle of 0° . The saturation profiles predicted at different times demonstrate that variations in fluid viscosity ratio significantly influence the invading velocity and saturation distribution within the tube.

2.2.2. Dynamic Network Model With Critical Capillary Number

By comparing Equation 8 with Equation 17, the volumetric flow rate of corner flow (q_c) at initial position ($x = 0$) is expressed as:

$$q_c = -BS^n \frac{\partial(SCR^2)}{\partial x} \Big|_{x=0} = CR^2 BS_0^n \frac{aS_0}{nx_f} = aCR^2 \left(\frac{B}{2nK_0 t} \right)^{1/2} \quad (22)$$

The volumetric flow rate of main-meniscus flow is calculated as $q_{MTM} = -K_{ij,w}(P_{i,w} - P_{j,w})$, and local capillary number ($Ca = \mu q/A\sigma$) is introduced to quantify the main-meniscus flow ($q_{MTM} = A\sigma Ca/\mu_w$), where the wetting fluid fully occupies the cross-section. Thus, the flow rate ratio between corner flow and main-meniscus flow is obtained:

$$\frac{\int q_c dt}{\int q_{MTM} dt} = \frac{aC \left(\frac{2B'}{nk_0} \right)^{1/2} R^2}{CatA\sigma/\mu_w} = \frac{CR^2}{A} \quad (23)$$

The critical capillary number is defined as:

$$Ca_c = \frac{a \left(\frac{2B'}{nk_0} \right)^{1/2}}{(3R\sigma\tau/\mu_w)^{1/2}} = \frac{a \left(\frac{2B'}{nk_0} \right)^{1/2}}{(3\tau)^{1/2}} = a \sqrt{\frac{2B'}{3\tau n K_0}} \quad (24)$$

where $B' = \frac{B\mu_w}{R\sigma} = \frac{\hat{\rho}_w}{C} m_1$ and the dimensionless time $\tau = t\sigma/3\mu_w R$.

To validate the dynamic network model incorporating Equation 24, two benchmark simulations are performed in a horizontal square tube with a diameter of 500 μm , separately analyzing main-meniscus flow and corner flow. The fluid properties used in the simulations are based on the work of Dong and Chatzis (1995). The nonwetting fluid viscosity is fixed as $\mu_n = 0.02 \text{ mPa} \cdot \text{s}$ and the wetting fluid viscosity varies from 0.02 $\text{mPa} \cdot \text{s}$

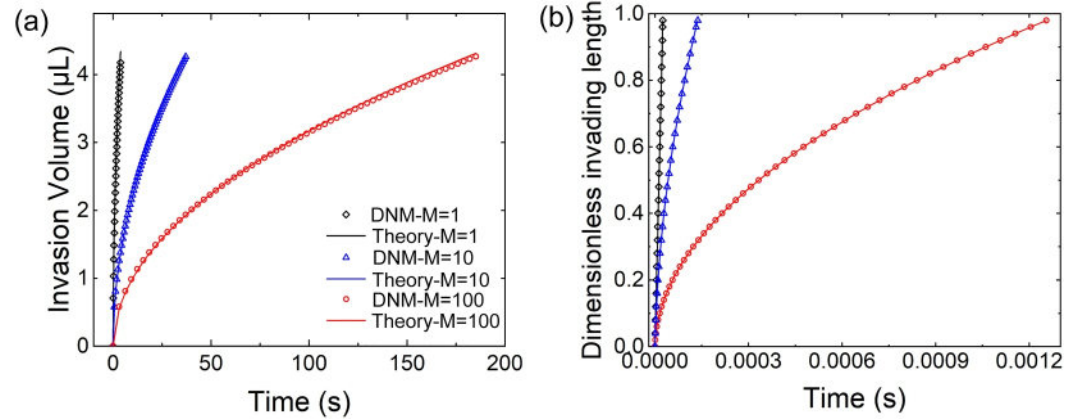


Figure 3. Comparison of the positions of the imbibition front at various times in a 500- μm square capillary tube with theoretical predictions: (a) Contact angle $\theta = 0^\circ$ (only corner flow occurs); (b) Contact angle $\theta = 60^\circ$ (only main-meniscus flow occurs). The viscosity ratio $M = \mu_w/\mu_n$ varies from 1 to 100.

to 2 mPa·s. The interface tension is set as $\sigma = 72$ mN/m. To isolate the interfacial dynamics of each flow regime, the contact angle is set to 0° , where capillary forces dominate over viscous forces, promoting wetting film formation along the tube corners. In contrast, a contact angle of 60° is used in the square tube, where geometric constraints ($\theta + \beta < \pi/2$) suppress corner flow, allowing only main-meniscus flow to occur. The theoretical solution of the total volume V_t during corner flow, imbibed at time t , is derived by integration of Equation 22:

$$V_t = a_0 C R^2 \left(\frac{2Bt}{nK_0} \right)^{1/2} \quad (25)$$

The comparison of the spontaneous imbibition front in a square capillary tube denotes that the modeling results match well with the corresponding theoretical predictions (Figure 3). The theoretical analysis of main-meniscus flow is given in Appendix D.

Employing this mathematical model (Ca_c) of pore-scale interfacial event, an improved DNM is established in this study:

1. Identifying the connected pores: We first identify and label pores that are fully saturated with the wetting fluid and are connected to neighboring pores that do not contain wetting fluid ($S_w = 0$).
2. Computing the local capillary number: The local capillary number of the invading wetting fluid is calculated for the identified pore pairs. This capillary number characterizes the dynamic competition between capillary forces and viscous forces at the interface.
3. Determining the interfacial event: When the local capillary number in the upstream pore (which is already invaded by wetting fluid) falls below the critical capillary number (Ca_c) of the downstream pore ($S_w = 0$), the wetting fluid advances via corner flow. Otherwise, the fluid progresses via main-meniscus flow.

3. Results and Discussion

3.1. Competition Between Main-Meniscus and Corner Flow in Pore-Throat Channel

The corner flow along the angular spaces tends to merge, resulting in an interface instability known as the snap-off event in a rectangular tube, which is subject to the following geometrical constraint (Lei, Lu, et al., 2023):

$$\cos \theta \left(\frac{1}{W_p} + \frac{1}{d_p} \right) < \frac{\cos \theta - \sin \theta}{\min(W_t, d_t)} \quad (26)$$

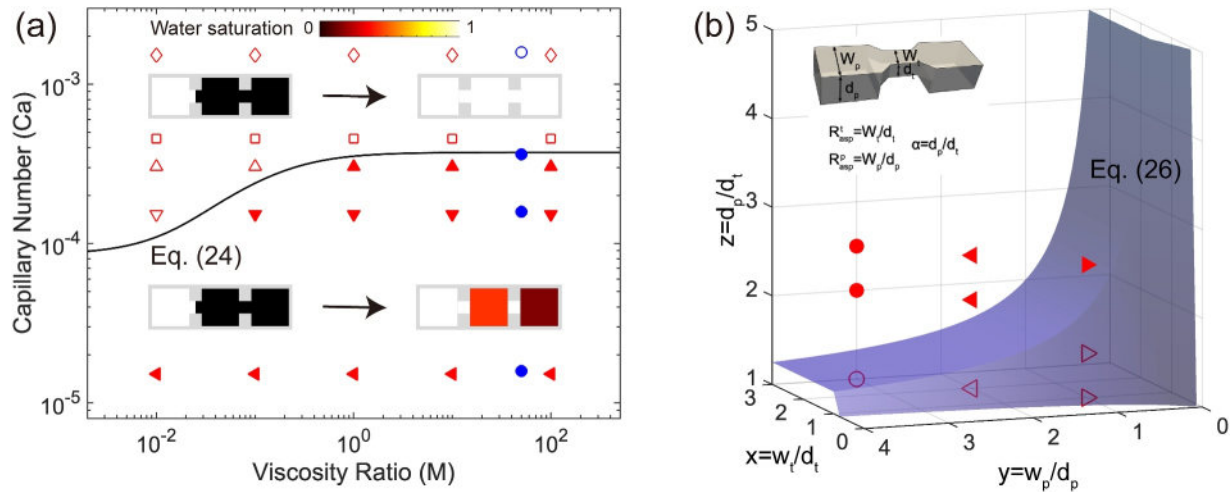


Figure 4. The phase diagram of pore-scale interfacial dynamics: (a) transition from main-meniscus flow to corner flow; (b) transition from corner flow to main-meniscus flow. The hollow and solid markers denote the occurrence and inexistence of the interfacial events. The red and blue markers represent the numerical cases under various capillary numbers ($Ca = 1.52 \times 10^{-3}, 1.52 \times 10^{-4}, 3.04 \times 10^{-4}, 4.56 \times 10^{-4}, 1.52 \times 10^{-5}$). The solid line in (a) represents Equation 24, and (b) is adapted from Lei et al.'s work (Lei, Lu, et al., 2023). Subfigure (b) illustrates the morphology of the pore-throat channel, showing the pore width and depth (W_p, d_p) as well as the throat width and depth (W_t, d_t). The aspect ratios of pore and throat are denoted as R_{asp}^p and R_{asp}^t , respectively. The blue surface, predicted by Equation 26, represents the onset condition for the snap-off event.

where W_p and d_p are the width and depth of pore body, and W_t and d_t for the width and depth of the pore throat. For a pore throat that satisfies Equation 26, a snap-off event may occur if the local capillary pressure is below the critical threshold given in Equation 6. Conversely, if a pore throat does not satisfy Equation 26, the snap-off event is not allowed, even when the local capillary pressure is low. To validate the application of microscopic rules in DNM, Equation 24 (transition from main-meniscus flow to corner flow) and Equation 26 (transition from corner flow to main-meniscus flow) are tested in a pore-throat channel. The competition between main-meniscus flow to the corner flow is verified in a network with square cross-section ($W_p = d_p$ and $W_t = d_t$). The sizes of pore body and pore throat are 500 and 250 μm , respectively. The forced imbibition is simulated for multiphase fluids with viscosity ratios $M = 0.01, 0.1, 1, 10,$ and 100 (labeling as red markers). The wetting fluid is injected under different capillary numbers ($Ca = 1.5 \times 10^{-2}, 1.5 \times 10^{-3}, 1.5 \times 10^{-4}, 1.5 \times 10^{-5},$ and 1.5×10^{-6}). During the forced imbibition, the multiphase interface at the inlet remains the main-meniscus pattern. Additionally, a group of direct numerical simulations for water-gas forced imbibition process using volume of fluid method are compared in Figure 4a, and the case points are labeled as blue markers (viscosity ratio $M = 54.8$). The details of direct numerical simulation method can be referred in Lei et al. (2024). The hollow marker represents that the wetting fluid invades the pore structure with main-meniscus flow and the corner flow is suppressed. The solid marker indicates the onset of corner flow, and the solid line describes the variation of critical capillary number under different viscosity ratios following Equation 24. The tests of forced imbibition under various capillary numbers and viscosity ratios demonstrate the DNM with the critical capillary number captures the transition from main-meniscus flow into corner flow in a pore-throat channel. For the verification on transition from corner flow into main-meniscus flow, the water is injected to displace the gas in a network with different size ratios (d_p/d_t) and aspect ratios (W/d). The capillary number is set as $Ca = 1.5 \times 10^{-6}$ to promote the occurrence of corner flow. The aspect ratio of pore body and pore throat remains consistent and varies as 1, 2, and 3 (labeling as circle, left triangle, and right triangle, respectively). The size ratios are chosen as 1, 2, and 2.5, respectively. As shown in Figure 4b, the hollow marker denotes that the wetting fluid remains the corner flow pattern in a throat, and the solid marker for the occurrence of snap-off event. Equation 26 provides the geometrical constraints for size ratio, aspect ratio of pore body and aspect ratio of pore throat, which is depicted by a curved surface (dark blue surface in Figure 4b). The results reflect that our DNM incorporating the geometrical constraints can also capture the transition from corner flow to main-meniscus flow.

3.2. Validation of Forced Imbibition Pattern in Porous Media

To further validate the new dynamic network model (DNM) presented in this study, we compared our numerical results with published microfluidic experiments. These experiments provide insight into pore-scale interfacial dynamics including main-meniscus flow and corner flow and their impact on macroscopic displacement patterns, particularly in water-gas systems with large viscosity ratios. To assess the impact of 3D pore geometry on these interfacial dynamics, we utilized porous structures reconstructed from microfluidic models developed in Lei et al. (2024), which feature varying pore depths achieved through one to three etching cycles. These correspond to depth variation factors $D_\alpha = 1, 2, 3$. Pore networks were extracted using the SNOW algorithm (Gostick, 2017), and the influence of pore depth variation on flow properties was characterized through single-phase network simulations, as shown in Figure A1 of Appendix A. The reconstructed networks serve as a platform for analyzing dynamic competition between main-meniscus flow and corner flow under different injection conditions.

The published experiments investigated forced imbibition in porous media with varying depth factors ($D_\alpha = 1, 2, 3$) across a wide range of capillary numbers ($Ca = \mu u / \sigma$), spanning from 2.6×10^{-7} to 2.6×10^{-4} . The results demonstrated that the imbibition pattern is influenced by both Ca and the structural depth variation of the porous medium (Figure B1 in Appendix B). The transition from complete to incomplete displacement predominantly occurs at lower Ca and higher depth variation factor. In porous media with $D_\alpha = 1$, interfacial instability emerges during forced imbibition, particularly at low Ca . This behavior is governed by pore-scale interfacial events, including the transition between main-meniscus flow and corner flow, as well as snap-off event and an increased trapping of nonwetting phase droplets. Conversely, at high Ca , the interface advances primarily as a main-meniscus flow pattern, as the transition to corner flow is suppressed.

Previous pore-scale models often assumed the presence of a wetting film during imbibition, minimizing the role of corner flow in displacement dynamics (He et al., 2021; Joekar-Niasar, Prodanović, et al., 2010; Joekar-Niasar & Majid Hassanizadeh, 2011; Li et al., 2017; Qin and van Brummelen, 2019; Thompson, 2002). Recent work introduced a capillary-driven criterion for the onset of corner flow, which states that this transition occurs when the local capillary pressure in upstreaming pore with main-meniscus flow exceeds the entry capillary pressure of the adjacent pore, as defined by the MS-P theory (Qin and van Brummelen, 2019). Integrating this criterion into the dynamic network model (Qin and van Brummelen, 2019), we use this previous model to investigate forced imbibition in porous media with various depth factors. Comparing with microfluidic experiments highlights the importance of the interplay of interfacial dynamics, which previous models have overlooked. Water saturation distribution predicted by previous model are characterized at breakthrough state (Figure B2), defined as the moment the wetting phase reaches the outlet. However, simulations based on the previous model failed to capture the incomplete interfacial pattern observed experimentally in porous media with $D_\alpha = 3$ at low Ca . This limitation arises because the previous model determines the onset of corner flow solely by comparing local capillary pressure and entry capillary pressure, without accounting for the influence of viscous forces on interfacial dynamics (Qin and van Brummelen, 2019). Yet, a visual comparison of interfacial patterns (Figures B1 and B2) suggests that displacement mechanisms in structures with varying depth require a broader framework. Further research is needed to fully understand the onset and evolution of interfacial dynamics, particularly the competition between main-meniscus and corner flow.

By integrating a critical capillary number into dynamic network model, we successfully captured these transitions in our numerical simulations (Figure B3), achieving strong agreement with the experimental observations (Figure B1). In subfigures Figures B3a–B3l, the white areas indicate that the pores are almost occupied by wetting phase, attributed to the main-meniscus flow where the wetting fluid completely displaces the nonwetting fluid in the local pore structure. The black areas represent pores with minimal wetting fluid, corresponding to the corner flow, where the wetting fluid invades the pore structure along the angular corners. The DNM modeling results indicate a transition of interfacial patterns from main-meniscus flow to corner flow. At low Ca , capillary forces dominate over viscous forces, frequently triggering corner flow events, as governed by the critical capillary number. A similar effect occurs when depth variation increases: the expansion of local pore structures reduces viscous resistance, shifting the balance further in favor of capillary forces and enhancing the onset of corner flow. This results in lower water saturation within the local pore structure. The dominant interfacial patterns, including both main-meniscus and corner flow, are presented in Figures B3a and B3l.

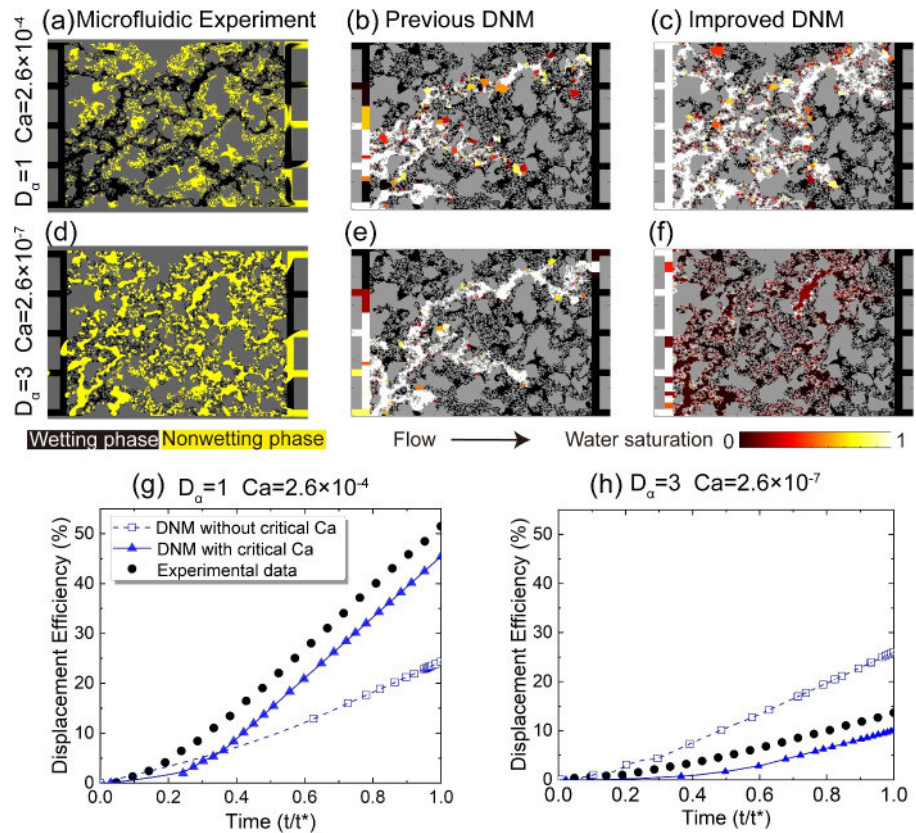


Figure 5. Comparison of water-gas displacement during forced imbibition in porous media. (a–c) For the spatial distribution of water and gas in porous media with $D_a = 1$ at high capillary number ($Ca = 2.6 \times 10^{-4}$) from the microfluidic experiments, previous model, and DNM incorporating critical capillary number; (d–f) for the porous media with $D_a = 3$ at low capillary number ($Ca = 2.6 \times 10^{-7}$). (g, h) Are the temporary variation of displacement efficiency under the corresponding multiphase flow conditions.

Comparison of temporary variation of water saturation during forced imbibition, as obtained from experimental results, the previous model, and the DNM incorporating the critical capillary number, was conducted under the injection conditions of Figures B1a and B11, as shown in Figure 5. The results indicate that while the DNM incorporating the critical capillary number underpredicts water saturation observed in microfluidic experiments, it provides a more accurate representation of the imbibition process compared to the model without the critical capillary number. This critical capillary number, which balances the local flux of the wetting fluid under the interplay of viscous and capillary forces, effectively captures the transition from stable to ramified interfacial displacement. This transition is attributed to dynamic competition between main-meniscus flow and corner flow in heterogeneous porous media, as supported by previous experimental observations in structures with varying depth variation factors (Lei, Lu, et al., 2023).

3.3. A New Insight to Lenormand's Phase Diagram

Lenormand's phase diagram, which maps capillary and viscous fingering as a function of Ca and M , traditionally focus on main-meniscus flow, where capillary-dominated invasion favors entry into small pores during imbibition, while viscous forces promote flow along preferred flow paths. However, this framework does not consider the role of corner flow, which plays a crucial role in imbibition processes. This study investigates forced imbibition under varying Ca and M and extends the understanding of interfacial patterns beyond those captured by Lenormand's diagram. Unlike drainage, where the competition between capillary and viscous fingering primarily determines the displacement efficiency, forced imbibition exhibits an additional complexity due to the competition between main-

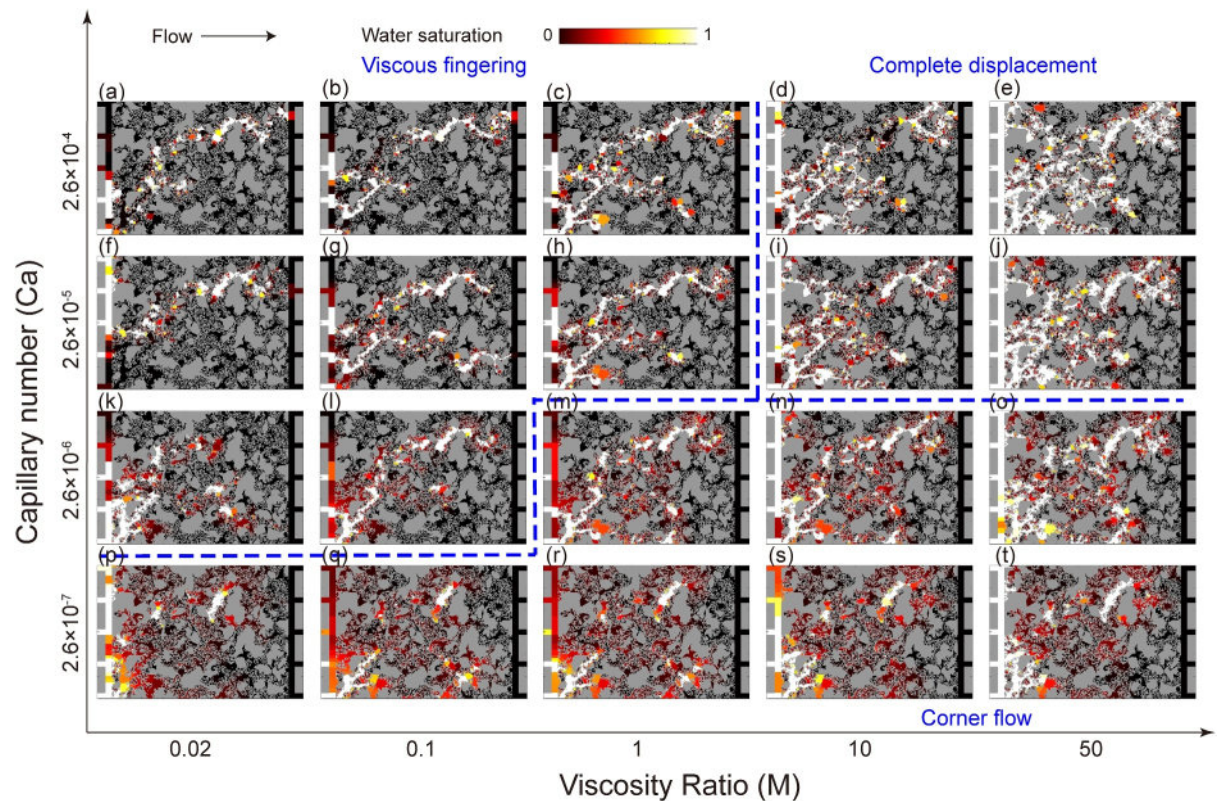


Figure 6. The dynamic network modeling results for the forced imbibition in porous media with uniform depth ($D_a = 1$) under various capillary numbers and fluid viscosity ratios. The blue dash line divides the forced imbibition pattern based on saturation morphology of the wetting phase.

meniscus flow and corner flow. The transition between these two displacement modes is governed by a critical capillary number (Ca_c), which depends on the local interplay of capillary and viscous forces.

Figure 6 illustrates the impact of Ca and M on the competition between corner flow and main-meniscus flow during forced imbibition. At a low Ca and a low M , corner flow is the dominant displacement mechanism, as indicated by extensive dark red regions in the saturation maps (Figure 6p). As Ca increases at $M = 0.02$ (Figures 6a, 6f, 6k and 6p), the interfacial pattern gradually transitions from corner flow to main-meniscus flow due to the enhanced influence of viscous forces. However, the number of displacement pathways also decreases under these conditions, resulting in fewer active invasion paths and the emergence of limited viscous fingering at a high Ca . In contrast, at a high M (e.g., $M = 50$), the number of displacement pathways remains relatively constant as Ca increases (Figures 6e, 6j, 6o and 6t). Nevertheless, the local interfacial pattern still undergoes a transition from corner flow to main-meniscus flow as Ca increases, driven by the suppression of capillary forces. These observations suggest that while the capillary number primarily governs the interfacial pattern, the viscosity ratio strongly influences the connectivity and extent of the invasion pathways during displacement. Besides, at a high Ca (Figures 6a–6e), the displacement pattern is dominated by main-meniscus flow, and the wetting-phase saturation increases significantly, resulting in more continuous displacement pathways. To further interpret the interfacial displacement behaviors captured by the dynamic network model (DNM), the flow patterns observed in the simulations are qualitatively classified into three distinct regimes: viscous fingering, complete displacement, and corner flow. These regimes are distinguished based on the morphology of water saturation maps and their dependence on capillary number (Ca) and viscosity ratio (M). The classification is visually represented in Figure 6, with dashed blue lines delineating qualitatively the boundaries between the regimes. A more detailed description of the classification criteria, along with supporting statistical evidence (Figure E1), is provided in Appendix E.

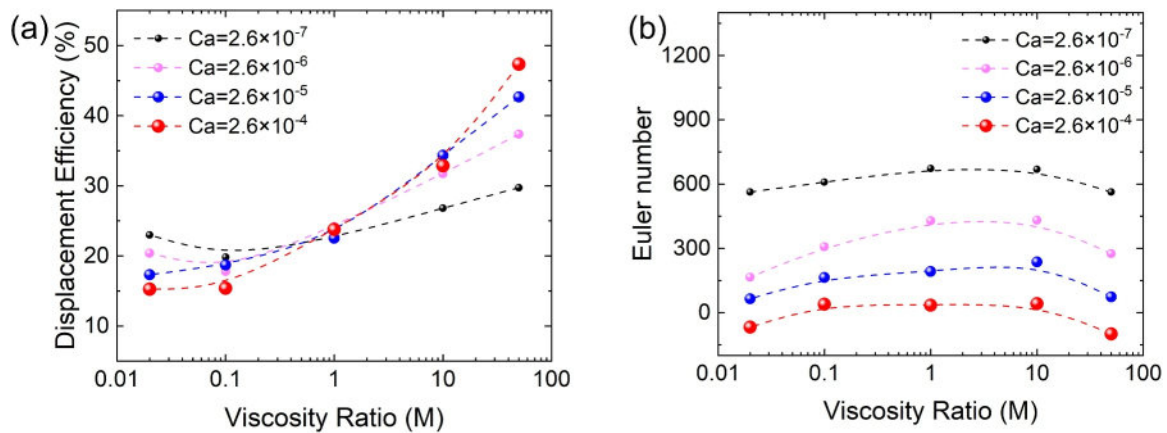


Figure 7. Effect of viscosity ratio on the multiphase displacement behavior at breakthrough state during the forced imbibition in porous structure with uniform depth ($D_c = 1$) using the dynamic network model: (a) displacement efficiency; (b) Euler number of the wetting fluid.

To assess the influence of Ca and M on displacement efficiency, two key parameters are employed in the DNM-based simulation analysis: displacement efficiency and the Euler number of the wetting phase (Figure 7). Displacement efficiency, defined as the ratio of the wetting-phase volume to total pore volume, reflects the overall saturation of the porous medium. The Euler number, which characterizes the topology of the wetting phase in porous media, is defined as the total number of fluid clusters minus the sum of the number of holes and cavities within those clusters. In a planar porous structure, the cavities within fluid clusters are ignored. A lower Euler number for the wetting fluid path indicates that the wetting fluid encompasses more solid particles and occupies a greater number of pores with fewer discrete fluid clusters, signifying enhanced connectivity. This calculation is performed using a Fiji plugin, MorphoLibJ (Legland et al., 2016). The displacement efficiency increases monotonically with viscosity ratio under high Ca , while it exhibits non-monotonic variation under low Ca . The non-monotonic variation of Euler number in Figure 7b shows lower values at both high and low viscosity ratio compared to a uniform viscosity ratio. This reflects that the discrepancy between the number of fluid clusters and the number of solid particles encompassed by the wetting fluid is more pronounced at high or low viscosity ratios.

At a high M , a higher critical capillary number predicting the local interfacial dynamics leads to a more frequent occurrence of corner flow during forced imbibition in porous media at low Ca . The increase in corner flow events at high M is influenced by two factors: the invasion of fluid into new pores, and the transition of interfacial pattern from main-meniscus flow to corner flow. The fluid invasion into new pores creates additional displacement paths, which increases wetting-phase saturation. Conversely, the transition from main-meniscus flow to corner flow reduces wetting-phase saturation in local pores. The ultimate saturation in the entire porous structure is determined by the competition between the corner flow invading new pores and the transition from main-meniscus flow. At a low Ca , the wetting fluid invasion is primarily governed by corner flow due to the dominance of capillary forces. As the viscosity ratio (M) increases, the critical capillary number (Ca_c) also rises, allowing more pores to meet the condition $Ca < Ca_c$ and thus favoring corner flow. This leads to an increasing proportion of corner flow events across the medium. While corner flow generally promotes higher wetting-phase saturation through film-like propagation, the transition of interfacial pattern from main-meniscus flow to corner flow in certain pore geometries may reduce saturation locally. This interplay explains the non-monotonic variation of overall wetting-phase saturation observed for $Ca = 2.6 \times 10^{-7}$ as M increases from 0.01 to 100. At high Ca , the forced imbibition process is dominated by complete displacement patterns, and corner flow is suppressed due to the impact of viscous forces, resulting in a slight impact on fluid saturation. Consequently, the monotonic variation in wetting-phase saturation is more relevant with the occurrence of compact displacement at high viscosity ratios.

4. Conclusions

This study explores the dynamic competition between main-meniscus flow and corner flow during forced imbibition in porous media. A critical capillary number (Ca_c) is proposed to capture the transition between these flow regimes under various capillary numbers (Ca) and viscosity ratios (M) based on the local balance between capillary and viscous forces. This criterion is incorporated into a dynamic network model (DNM), which is validated against microfluidic experiments and theoretical predictions.

Simulation results demonstrated that transition of the dominant interfacial pattern from main-meniscus flow to corner flow was captured using the presented DNM framework. At high Ca , viscous fingering dominates, leading to a monotonic increase in displacement efficiency with viscosity ratio. In contrast, at low Ca , viscosity ratio exhibits a non-monotonic effect: displacement efficiency is reduced at low M due to corner flow events, while high M promotes pore connectivity by enabling wetting-phase advancement through corners. These findings underscore the significant role of local interfacial dynamics in shaping macroscopic displacement behavior.

This work provides new insights into pore-scale interfacial dynamics and their macroscopic implications, offering a physically grounded approach for incorporating interfacial phenomena into pore-scale modeling. While the study primarily focuses on strong imbibition under fixed wettability conditions, future work would explore the influence of wettability and additional interfacial behaviors such as viscous instability and Haines jumps, particularly in 3D porous structures.

Appendix A: The Structure Characteristics of Porous Media

The porous structures used in this study were reconstructed using quartet structure generation set (QSGS) method (Lei et al., 2020). Owing to the uniform pore depth in the microfluidic porous structure, the hydraulic radius of local pore spaces with rectangular cross-section ($r_h = 0.5Wd/(W + d)$, where W and d are the width and depth of the cross-section) is truncated, specially, for larger pores. This leads to a discrepancy between the pore size distribution of the 2D porous structure (width distribution) and that of the (three-dimensional) 3D porous structure (hydraulic diameter distribution). As illustrated in Figure A1, three types of porous structures with different pore depths were designed to introduce 3D pore size variations. In the microfluidic model etched once, all pores have a uniform depth of 40 μm . With two etching cycles, pores in regions with planar radii exceeding 40 μm extend to a depth of 80 μm . Similarly, in the model etched three times, pores larger than 80 μm in size extend to a depth of 120 μm . To characterize these structures, the depth variation factor (D_α), based on the number of etching cycles, is set to 1, 2, and 3 for models with depths of 40, 80, and 120 μm , respectively. The pore size distributions for the different depth models are calculated and shown in Figures A1d–A1f. The corresponding network were extracted using the SNOW algorithm (Gostick, 2017), and the pore spaces were categorized into three groups, pores with radii smaller than 40 μm (red part), those larger than 120 μm (green part), and the remaining pores (yellow part), as shown in Figures A1a–A1c. The fabrication details in microfluidic model can be referred in Lei et al.'s work (2024).

The variation in the depth of local pores results in geometrical difference in the 3D porous structure, such as pore volume and equivalent pore size, which is also reflected in the flow properties including fluid conductance and local capillary pressure. A single-phase pore-network model is used to solve the Hagen-Poiseuille equation within the networks under a constant pressure difference. The results show a significant sensitivity of flow rates in porous media to the depth variation (Figures A1g–A1i). It is noted that the flow rate is represented by the volumetric rate of fluid entering the pore body. Comparison of flow fields reveals that the increase in volumetric flow rate is most pronounced in the enlarged pores of the porous medium with a depth variation factor ($D_\alpha = 3$) (highlighted in green in Figure A1c). The corresponding permeabilities for each network, calculated using Darcy's law $k = \frac{\mu QL}{\Delta PA}$, are $k(D_\alpha = 1) = 2.9 \times 10^{-12}$ m², $k(D_\alpha = 2) = 4.3 \times 10^{-12}$ m², and $k(D_\alpha = 3) = 7.1 \times 10^{-12}$ m², where fluid viscosity $\mu = 1$ mPa \cdot s and pressure difference $\Delta P = 1000$ Pa. In the following sections, these networks of porous structures with different depths are employed to investigate the competition between interfacial dynamics under various injection conditions.

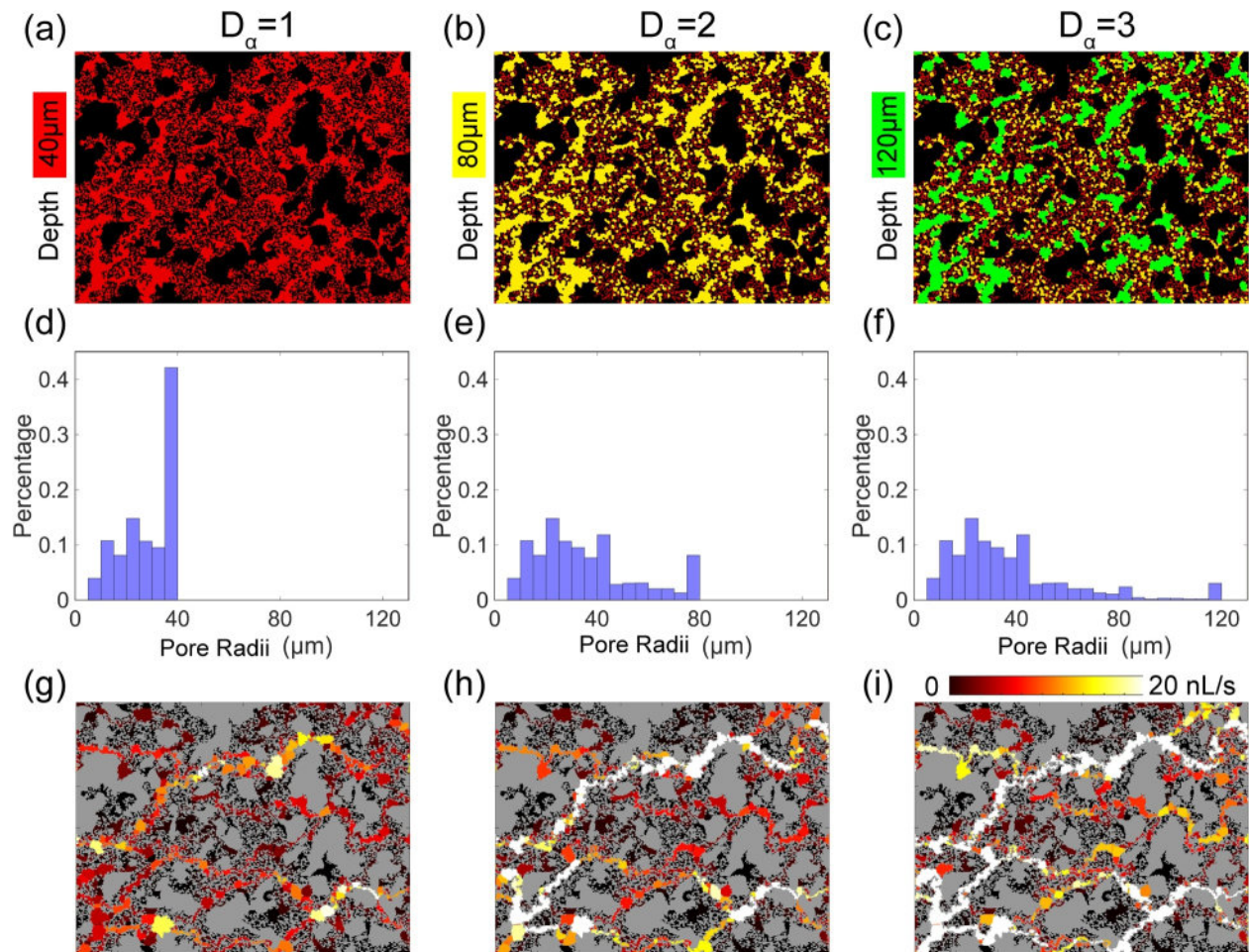


Figure A1. Characterization of porous media with uniform topology and different depths ($D_\alpha = 1, 2, 3$): (a–c) for the pore depth distribution; (d–f) for the hydraulic radius distribution; (g–i) for the fluid velocity distribution, defined as the volumetric rate in each pore body.

Appendix B: Phase Diagram of Water-Gas Forced Imbibition in Microfluidic Experiments

The microfluidic experiments of water-gas displacement were conducted in the porous structure models with different depth variation factors introduced in Section 3.2 (Figure A1). The microfluidic chip is fabricated using silicon material with different etched times. In the microfluidic experiments of forced imbibition, the viscosities of water and gas are $1 \text{ mPa} \cdot \text{s}$ and $1.825 \times 10^{-2} \text{ mPa} \cdot \text{s}$. The interface tension and contact angle of water-gas on the pore wall are measured as 72 mN and 10° . The wetting fluid (water) was injected into the microfluidic porous model fully saturated by the nonwetting fluid (air) with a constant flux rate. The capillary number varies from 2.6×10^{-7} to 2.6×10^{-4} . The temporary evolution of the displacement behaviors was recorded by a Nikon camera. The spatial distributions of water and gas in porous media at breakthrough state are displayed in Figures B1–B3 for experiments and numerical data from previous DNM and the improved DNM, respectively. Details of the microfluidic chip fabrication and forced imbibition experimental operation are referred in our previous work (Lei, Lu, et al., 2023).

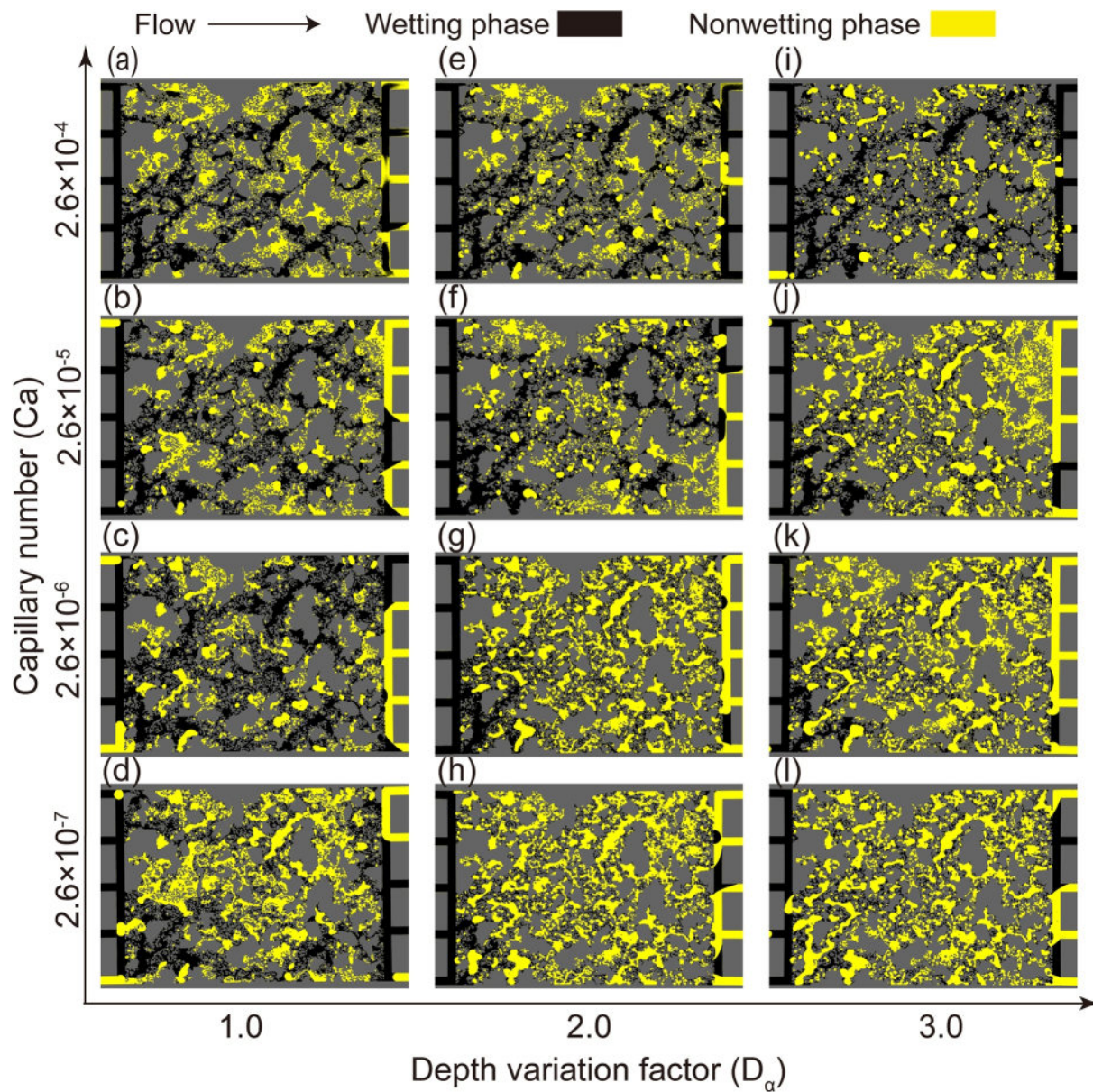


Figure B1. The microfluidic experiments of water-gas displacement in porous media with different depths under various capillary numbers (Lei, Lu, et al., 2023), where the black part represents the pore space occupied by wetting phase, yellow part for nonwetting phase, and gray part for solid matrix.

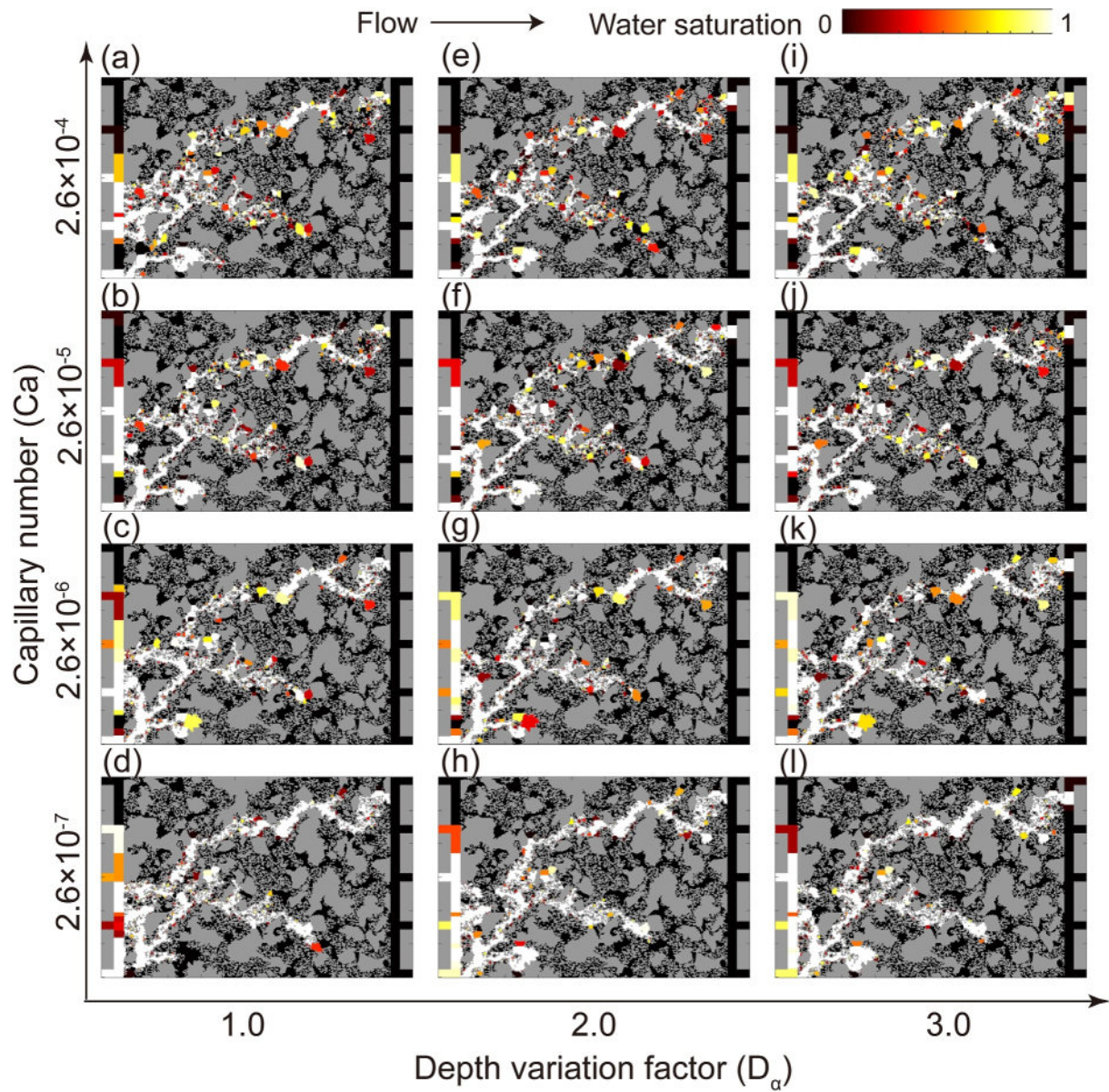


Figure B2. The numerical results of water saturation distribution during water-gas forced imbibition in porous media with different depths under various capillary numbers using the dynamic network model.

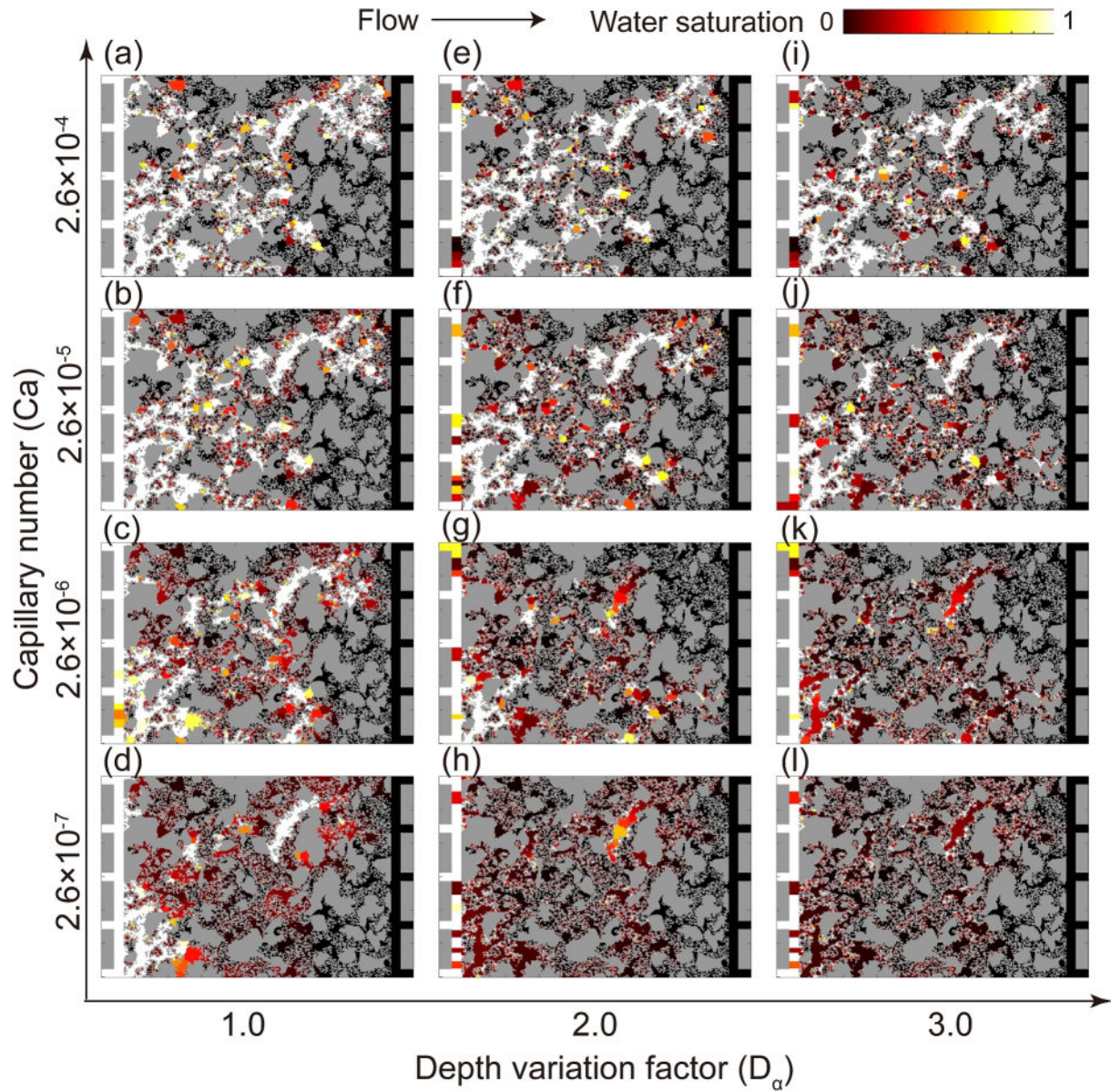


Figure B3. The numerical distributions of water saturation during water-gas forced imbibition in porous media with different depths under various capillary numbers using the improved DNM.

Appendix C: Approximation of the Polynomial

Figure C1 presents the approximation of the polynomial of wetting fluid saturation $m_0 S^{1/3} + S^{1/2}$, where $m_0 \left(= \frac{74}{8.6 + e^{2.54\mu}} \right)$ is a function of fluid viscosity ratio. Due to the challenges in the integration of multiple powerful functions, this polynomial is treated as a single power function mS^n , where parameters m and n are introduced as $m_1 = m_0 + e^{-0.03m_0}$ and $m_2 = 1/3 + e^{-m_0}/6$. Herein, the exponential function of fluid viscosity is used to constrain the range of parameters ($m_0 < m_1 < m_0 + 1, 1/2 < m_2 < 1/3$) for the dimensionless saturation varying from 0 to 1. The data from these two functions of dimensionless saturation matches well with the linear curve $y = x$, and the average relative error is 3.75%. In the comparison, the viscosity ratio varies from 0.001 to 1000, and dimensionless saturation ranges from 0.01 to 0.6. The error of individual approximation is reflected in Figure B1b.

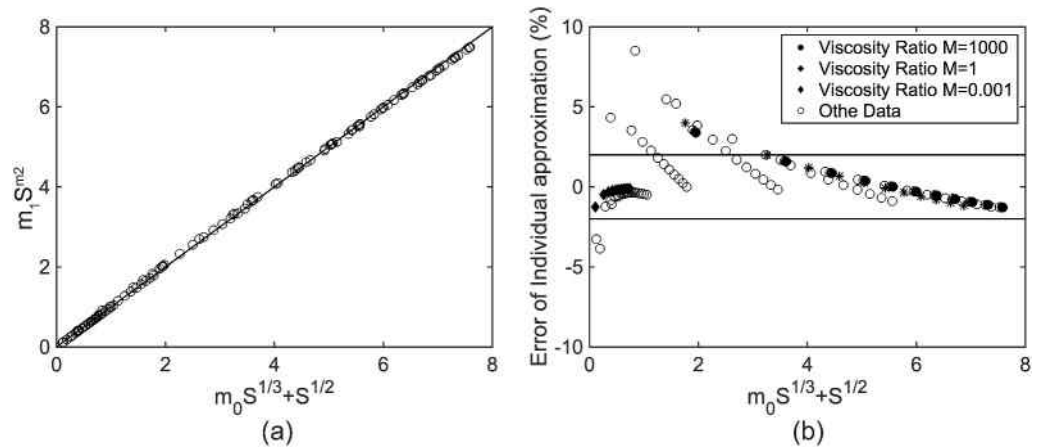


Figure C1. Approximation for the polynomial of wetting fluid saturation $m_0 S^{1/3} + S^{1/2}$: (a) comparison of approximation; (b) relative error of individual approximation. The averaged relative error of approximation is 3.75%.

Appendix D: The Theoretical Solution of Main-Meniscus Front under Various Viscosity Ratios

The main-meniscus front during spontaneous imbibition within a regular capillary tube placed along the horizontal direction could be predicted by balancing the capillary force and viscous resistance. The capillary force (P_c) is calculated using Young-Laplace equation, and the viscous resistance (P_v) follows the derivation in the Patzek et al.'s work.

$$P_c - P_v = 0 \quad (D1)$$

$$P_c = \frac{2\sigma \cos \theta}{R} \quad (D2)$$

$$P_v = \frac{u[\mu_w x + \mu_n(L - x)]}{\chi GA} \quad (D3)$$

where the main-meniscus front invades the tube with the total length L and cross-section are A , the invading velocity is $u = dx/dt$ at the position of wetting-fluid length x . χ and G are the hydraulic coefficient and geometrical factor of the capillary tube, which is determined as 0.5623 and 1/16 for the square tube. The integration of the abovementioned equations yields the invading time t with the invading length of wetting fluid l :

$$t = \frac{\mu_w x^2 + \mu_n(2Lx - x^2)}{2P_c \chi GA} = \frac{\mu_n L^2}{2P_c \chi GA} \left[\left(\frac{\mu_w}{\mu_n} - 1 \right) \left(\frac{x}{L} \right)^2 + 2 \left(\frac{x}{L} \right) \right] \quad (D4)$$

Appendix E: Flow Pattern Classification in Forced Imbibition

To better understand the pore-scale interfacial dynamics during forced imbibition, three distinct flow patterns were identified in the dynamic network model (DNM) simulations by analyzing the morphology of water saturation maps and the corresponding statistical distribution of invaded pores. These patterns are distinguished based on the combined effects of capillary number (Ca) and viscosity ratio (M), and are demarcated in the Ca - M parameter space by dashed blue lines in Figure 6.

To support this qualitative classification, Figure E1 presents the number distribution of invaded pores (i.e., pores where the water saturation is greater than zero) at breakthrough state, allowing us to differentiate the extent and quality of pore invasion in each regime.

1. Viscous Fingering: the viscous fingering regime arises under low M and high Ca , where the injection front forms narrow, finger-like structures with limited connectivity. Most pores remain uninvaded, while the few that are

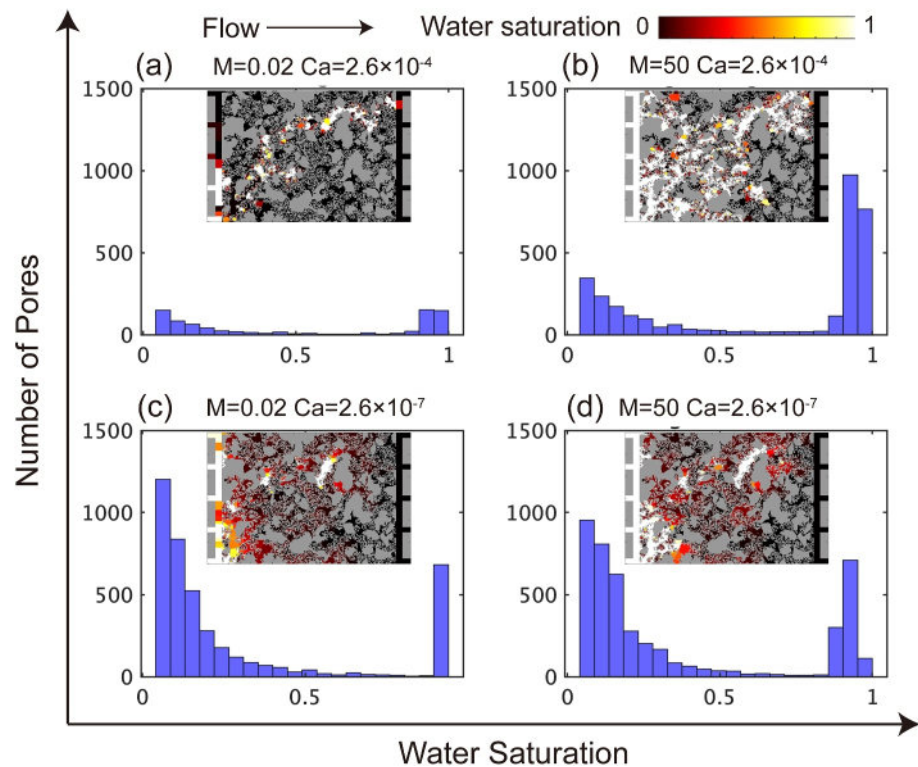


Figure E1. The water saturation distribution at breakthrough state for DNM results. The histogram presents the distribution of pore numbers injected by wetting phase and the colorful subfigures denotes the spatial distribution of water saturation.

- invaded reach very high saturation. A representative case is shown in Figure 6a, with $Ca = 2.6 \times 10^{-4}$ and $M = 0.02$. Correspondingly, Figure E1a displays a narrow distribution indicating that only a small number of pores are highly saturated.
2. Complete Displacement: the complete displacement regime is characterized by nearly uniform invasion of the wetting phase throughout the porous structure, with high saturation levels and dense, well-connected invasion pathways. This behavior is observed at high M and moderate-to-high Ca values, as illustrated in Figure 6e for $Ca = 2.6 \times 10^{-4}$ and $M = 50$. Figure E1b further confirms this regime by showing that the majority of pores are invaded and exhibit high water saturation.
 3. Corner Flow: the corner flow regime is observed at low M and low Ca , where the wetting phase invades through thin films along pore corners, resulting in extensive pore occupancy but generally low saturation in each pore. This leads to a highly branched and dispersed displacement front, as seen in Figure 6p for $Ca = 2.6 \times 10^{-7}$ and $M = 0.02$. Figure E1c supports this observation, showing a broad distribution of invaded pores, most of which maintain low water saturation.

This classification provides a foundational understanding of how local interfacial behaviors manifest in different macroscopic flow regimes, and forms the basis for delineating the flow zones in the Ca - M parameter space.

Nomenclature

Roman

a_0	A parameter introduced by the trial function
A_{ij}	The cross-section area in the pore throat ij
A_w	The area occupied by the wetting fluid
b	The film width in the cross-section

B	The replaced parameter. $B = \hat{g}_w \frac{\sigma R}{\mu_w C} m_1$
B'	The replaced parameter. $B' = \frac{\hat{g}_w}{C} m_1$
C	The geometric factor of the cross-section in the tube
d	The depth of the cross-section
d_p	The pore body depth
d_t	The pore throat depth
D_α	The depth variation factor
g_w	The hydraulic conductance of wetting fluid in the tube
\hat{g}_w	The dimensionless conductance of wetting fluid
G_{ij}	Shape factor for the pore throat ij
k	Permeability
K_0	A constant introduced by variation method
$K_{ij,\alpha}$	The hydraulic conductance of fluid α for the pore throat ij
l_{ij}	The length of pore throat ij
L	The total length of the tube
m_0, m_1, m_2	The fitting coefficients for viscous coupling effect
M	Viscosity ratio. $M = \mu_w / \mu_{nw}$
n	The power exponent of dimensionless saturation for the corner flow
N_i	The coordinate number of pore body i
$P_{i,\alpha}$	The pressure of fluid α in pore body i
P_i^c	The capillary pressure in pore body i
P_v	The viscous resistance
$P_{j,\alpha}$	The pressure of fluid α in pore body j
P_{ij}	The perimeter of the cross-section in the pore throat ij
$P_{ij,c}$	The capillary pressure in pore throat ij
q_c	The volumetric flow rate for corner flow
q_{MTM}	The volumetric flow rate for main-meniscus flow
q_w	The volumetric flow rate of the wetting fluid
$Q_{ij,\alpha}$	The flux of fluid α through the pore throat ij
$Q_{inlet,w}$	The wetting-fluid flux at inlet pores
r	The curvature radius of arc-meniscus
r_h	The hydraulic radius of local pore spaces
r_{ij}	The inscribed radius of the pore throat ij
R	The inscribed radius of the tube
S	The dimensionless saturation of corner flow
S_0	The initial dimensionless saturation of corner flow

$S_{i,\alpha}$	The saturation of fluid α in the pore body i
$S_{\text{inlet},w}$	The wetting-phase saturation at inlet pores
$S_{\text{outlet},w}$	The wetting-phase saturation at outlet pores
$S_{\text{outlet}-1,w}$	The wetting-phase saturation at the pores connecting to outlet pores
Δt	The time interval
t	The spreading time of the corner flow
u	Characteristic velocity of invading fluid
V_i	The pore volume of pore body i
V_t	The total volume of the corner flow
W_p	The pore body width
W_t	The pore throat width
W	The width of the cross-section
x	The location within the corner flow
x_0	The initial position of the corner flow
x_f	The front position of the corner flow during spreading

Greeks

α	The fluid phase ($\alpha = w, n$ for wetting and nonwetting phases)
β	The half angle of the cross-section
β_1	The half value of central angle for interface curvature
η	The viscous coupling coefficient
θ	The contact angle
μ_{in}	The dynamic viscosity of invading fluid
μ_{de}	The dynamic viscosity of defending fluid
μ_α	The dynamic viscosity of fluid α
$\hat{\mu}$	The logarithmic viscosity ratio ($-\log \frac{\mu_w}{\mu_n}$)
ν	The time constant. $\nu = K_0 \frac{\sigma r}{\mu_w \beta \lambda_0^2}$
σ	The interface tension
τ	The dimensionless time for corner flow
χ	The hydraulic conductance coefficient

Abbreviations

AD	automatic differentiation
Ca	capillary number
Ca_c	The critical capillary number

DNM	dynamic network model
QSGS	quartet structure generation set
2D	two-dimensional
3D	three-dimensional

Data Availability Statement

The code used in this work is implemented using the open-source MATLAB Reservoir Simulation Toolbox (MRST), developed primarily by the Applied Computational Science group in the Department of Mathematics and Cybernetics at SINTEF Digital (Bao, 2017). The library can be accessed at <https://www.sintef.no/projectweb/mrst/>.

References

- An, S., Erfani, H., Godinez-Brizuela, O. E., & Niasar, V. (2020). Transition from viscous fingering to capillary fingering: Application of GPU-based fully implicit dynamic pore network modeling. *Water Resources Research*, *56*(12), e2020WR028149. <https://doi.org/10.1029/2020WR028149>
- Anbari, A., Chien, H.-T., Datta, S. S., Deng, W., Weitz, D. A., & Fan, J. (2018). Microfluidic model porous media: Fabrication and applications. *Small*, *14*(18), 1703575. <https://doi.org/10.1002/smll.201703575>
- Armstrong, R. T., & Berg, S. (2013). Interfacial velocities and capillary pressure gradients during Haines jumps. *Physical Review E*, *88*(4), 043010. <https://doi.org/10.1103/PhysRevE.88.043010>
- Armstrong, R. T., Porter, M. L., & Wildenschild, D. (2012). Linking pore-scale interfacial curvature to column-scale capillary pressure. *Advances in Water Resources*, *46*, 55–62. <https://doi.org/10.1016/j.advwatres.2012.05.009>
- Bao, K. (2017). The MATLAB Reservoir simulation Toolbox: March 21, 2022 release (version MRST 2022a) [Software]. *MRST*. <https://www.sintef.no/projectweb/mrst/>
- Berg, S., Ott, H., Klapp, S. A., Schwing, A., Neiteler, R., Brussee, N., et al. (2013). Real-time 3D imaging of Haines jumps in porous media flow. *Proceedings of the National Academy of Sciences of the United States of America*, *110*(10), 3755–3759. <https://doi.org/10.1073/pnas.1221373110>
- Bultreys, T., Ellman, S., Schlepütz, C. M., Boone, M. N., Pakkaner, G. K., Wang, S., et al. (2024). 4D microvelocimetry reveals multiphase flow field perturbations in porous media. *Proceedings of the National Academy of Sciences*, *121*(12), e2316723121. <https://doi.org/10.1073/pnas.2316723121>
- Celia, M. A., Reeves, P. C., & Ferrand, L. A. (1995). Recent advances in pore scale models for multiphase flow in porous media. *Reviews of Geophysics*, *33*(S2), 1049–1057. <https://doi.org/10.1029/95RG00248>
- Cha, L., Xie, C., Feng, Q., & Balhoff, M. (2021). Geometric criteria for the snap-off of a non-wetting droplet in pore-throat channels with rectangular cross-sections. *Water Resources Research*, *57*(7), e2020WR029476. <https://doi.org/10.1029/2020WR029476>
- Chen, S., Qin, C., & Guo, B. (2020). Fully implicit dynamic pore-network modeling of two-phase flow and phase change in porous media. *Water Resources Research*, *56*(11), e2020WR028510. <https://doi.org/10.1029/2020WR028510>
- Chen, Y., Valocchi, A. J., Kang, Q., & Viswanathan, H. S. (2019). Inertial effects during the process of supercritical CO₂ displacing brine in a sandstone: Lattice Boltzmann simulations based on the continuum-surface-force and geometrical wetting models. *Water Resources Research*, *55*(12), 11144–11165. <https://doi.org/10.1029/2019WR025746>
- Cieplak, M., & Robbins, M. O. (1988). Dynamical transition in quasistatic fluid invasion in porous media. *Physics Review Letter*, *60*(20), 2042–2045.
- Dong, M., & Chatzis, I. (1995). The imbibition and flow of a wetting liquid along the corners of a square capillary tube. *Journal of Colloid and Interface Science*, *172*(2), 278–288. <https://doi.org/10.1006/jcis.1995.1253>
- Ebadi, M., McClure, J., Mostaghimi, P., & Armstrong, R. T. (2024). Bridging the gap: Connecting pore-scale and continuum-scale simulations for immiscible multiphase flow in porous media. *Physics of Fluids*, *36*(3), 033305. <https://doi.org/10.1063/5.0186990>
- Geistlinger, H., & Zulfikar, B. (2020). The impact of wettability and surface roughness on fluid displacement and capillary trapping in 2-D and 3-D porous media: I. Wettability-controlled phase transition of trapping efficiency in glass beads packs. *Water Resources Research*, *56*(10), e2019WR026826. <https://doi.org/10.1029/2019WR026826>
- Goirand, F., Le Borgne, T., & Lorthois, S. (2021). Network-driven anomalous transport is a fundamental component of brain microvascular dysfunction. *Nature Communications*, *12*(1), 7295. <https://doi.org/10.1038/s41467-021-27534-8>
- Gong, W., Liu, Y., Lei, W., Ju, Y., & Wang, M. (2023). Viscous coupling effect on hydraulic conductance in a square capillary tube. *Advances in Water Resources*, *182*, 104568. <https://doi.org/10.1016/j.advwatres.2023.104568>
- Gostick, J. T. (2017). Versatile and efficient pore network extraction method using marker-based watershed segmentation. *Physical Review E*, *96*(2), 023307. <https://doi.org/10.1103/PhysRevE.96.023307>
- He, M., Zhou, Y., Wu, K., Hu, Y., Feng, D., Zhang, T., et al. (2021). Pore network modeling of thin water film and its influence on relative permeability curves in tight formations. *Fuel*, *289*, 119828. <https://doi.org/10.1016/j.fuel.2020.119828>
- Holtzman, R., & Segre, E. (2015). Wettability stabilizes fluid invasion into porous media via Nonlocal, cooperative pore filling. *Physical Review Letters*, *115*(16), 164501. <https://doi.org/10.1103/PhysRevLett.115.164501>
- Hu, R., Zhou, C.-X., Wu, D.-S., Yang, Z., & Chen, Y.-F. (2019). Roughness control on multiphase flow in rock fractures. *Geophysical Research Letters*, *46*(21), 12002–12011. <https://doi.org/10.1029/2019GL084762>
- Joekar-Niasar, V., & Majid Hassanizadeh, S. (2011). Effect of fluids properties on non-equilibrium capillarity effects: Dynamic pore-network modeling. *International Journal of Multiphase Flow*, *37*(2), 198–214. <https://doi.org/10.1016/j.ijmultiphaseflow.2010.09.007>

Acknowledgments

This work is financially supported by the NSF grant of China (No. 52404049, 12432013) and Science Foundation of China University of Petroleum, Beijing (No. 2462024SZBH004).

- Joekar-Niasar, V., & Hassanizadeh, S. M. (2012). Analysis of fundamentals of two-phase flow in porous media using dynamic pore-network models: A review. *Critical Reviews in Environmental Science and Technology*, 42(18), 1895–1976. <https://doi.org/10.1080/10643389.2011.574101>
- Joekar-Niasar, V., Hassanizadeh, S. M., & Dahle, H. K. (2010). Non-equilibrium effects in capillarity and interfacial area in two-phase flow: Dynamic pore-network modelling. *Journal of Fluid Mechanics*, 655, 38–71. <https://doi.org/10.1017/s0022112010000704>
- Joekar-Niasar, V., Prodanović, M., Wildenschild, D., & Hassanizadeh, S. M. (2010). Network model investigation of interfacial area, capillary pressure and saturation relationships in granular porous media. *Water Resources Research*, 46(6). <https://doi.org/10.1029/2009WR008585>
- Ju, Y., Gong, W., Chang, W., & Sun, M. (2020). Effects of pore characteristics on water-oil two-phase displacement in non-homogeneous pore structures: A pore-scale lattice Boltzmann model considering various fluid density ratios. *International Journal of Engineering Science*, 154, 103343. <https://doi.org/10.1016/j.ijengsci.2020.103343>
- Ju, Y., Gong, W., & Zheng, J. (2022). Effects of pore topology on immiscible fluid displacement: Pore-scale lattice Boltzmann modelling and experiments using transparent 3D printed models. *International Journal of Multiphase Flow*, 152, 104085. <https://doi.org/10.1016/j.ijmultiphaseflow.2022.104085>
- Koplik, J., & Lasseter, T. J. (1985). Two-phase flow in random network models of porous media. *Society of Petroleum Engineers Journal*, 25(01), 89–100. <https://doi.org/10.2118/11014-pa>
- Lan, T., Hu, R., Yang, Z., Wu, D.-S., & Chen, Y.-F. (2020). Transitions of fluid invasion patterns in porous media. *Geophysical Research Letters*, 47(20), e2020GL089682. <https://doi.org/10.1029/2020GL089682>
- Legland, D., Arganda-Carreras, I., & Andrey, P. (2016). MorphoLibJ: Integrated library and plugins for mathematical morphology with ImageJ. *Bioinformatics*, 32(22), 3532–3534. <https://doi.org/10.1093/bioinformatics/btw413>
- Lei, W., Gong, W., Lu, X., & Wang, M. (2024). Fluid entrapment during forced imbibition in a multidepth microfluidic chip with complex porous geometry. *Journal of Fluid Mechanics*, 987, A3. <https://doi.org/10.1017/jfm.2024.358>
- Lei, W., Gong, W., & Wang, M. (2023). Wettability effect on displacement in disordered media under preferential flow conditions. *Journal of Fluid Mechanics*, 975, A33. <https://doi.org/10.1017/jfm.2023.879>
- Lei, W., Liu, T., Xie, C., Yang, H., Wu, T., & Wang, M. (2020). Enhanced oil recovery mechanism and recovery performance of micro-gel particle suspensions by microfluidic experiments. *Energy Science & Engineering*, 8(4), 986–998. <https://doi.org/10.1002/ese3.563>
- Lei, W., Lu, X., Gong, W., & Wang, M. (2023). Triggering interfacial instabilities during forced imbibition by adjusting the aspect ratio in depth-variable microfluidic porous media. *Proceedings of the National Academy of Sciences*, 120(50), e2310584120. <https://doi.org/10.1073/pnas.2310584120>
- Lei, W., Lu, X., Liu, F., & Wang, M. (2022). Non-monotonic wettability effects on displacement in heterogeneous porous media. *Journal of Fluid Mechanics*, 942, R5. <https://doi.org/10.1017/jfm.2022.386>
- Lenormand, R., Touboul, E., & Zarcone, C. (1988). Numerical models and experiments on immiscible displacements in porous media. *Journal of Fluid Mechanics*, 189, 165–187. <https://doi.org/10.1017/s0022112088000953>
- Lenormand, R., Zarcone, C., & Sarr, A. (1983). Mechanisms of the displacement of one fluid by another in a network of capillary ducts. *Journal of Fluid Mechanics*, 135, 337–353. <https://doi.org/10.1017/s0022112083003110>
- Li, D., Yang, Z., Pahlavan, A. A., Zhang, R., Hu, R., & Chen, Y.-F. (2024). Stability transition in gap expansion-driven interfacial flow. *Physical Review Letters*, 133(3), 034003. <https://doi.org/10.1103/PhysRevLett.133.034003>
- Li, J., McDougall, S. R., & Sorbie, K. S. (2017). Dynamic Pore-Scale Network Model (PNM) of water imbibition in porous media. *Advances in Water Resources*, 107, 191–211. <https://doi.org/10.1016/j.advwatres.2017.06.017>
- Li, Q., Yang, G., Huang, Y., Lu, X., Min, J., & Wang, M. (2024). Lattice Boltzmann method for particulate multiphase flow system. *International Journal of Mechanical Sciences*, 273, 109217. <https://doi.org/10.1016/j.ijmecsci.2024.109217>
- Liu, H., Kang, Q., Leonardi, C. R., Schmieschek, S., Narváez, A., Jones, B. D., et al. (2016). Multiphase lattice Boltzmann simulations for porous media applications. *Computational Geosciences*, 20(4), 777–805. <https://doi.org/10.1007/s10596-015-9542-3>
- Liu, Y., Gong, W., Zhao, Y., Jin, X., & Wang, M. (2022). A pore-throat segmentation method based on local hydraulic resistance equivalence for pore-network modeling. *Water Resources Research*, 58(12), e2022WR033142. <https://doi.org/10.1029/2022WR033142>
- Mansouri-Boroujeni, M., Soulaire, C., Azaroual, M., & Roman, S. (2023). How interfacial dynamics controls drainage pore-invasion patterns in porous media. *Advances in Water Resources*, 171, 104353. <https://doi.org/10.1016/j.advwatres.2022.104353>
- Patzek, T. W. (2001). Verification of a complete pore network simulator of Darinage and imbibition. *SPE Journal*, 6(02), 144–156. <https://doi.org/10.2118/71310-pa>
- Primkulov, B. K., Pahlavan, A. A., Fu, X., Zhao, B., MacMinn, C. W., & Juanes, R. (2021). Wettability and Lenormand's diagram. *Journal of Fluid Mechanics*, 923, A34. <https://doi.org/10.1017/jfm.2021.579>
- Qin, C.-Z., & van Brummelen, H. (2019). A dynamic pore-network model for spontaneous imbibition in porous media. *Advances in Water Resources*, 133, 103420. <https://doi.org/10.1016/j.advwatres.2019.103420>
- Raeni, A. Q., Bijeljic, B., & Blunt, M. J. (2017). Generalized network modeling: Network extraction as a coarse-scale discretization of the void space of porous media. *Physical Review E*, 96(1), 013312. <https://doi.org/10.1103/PhysRevE.96.013312>
- Raeni, A. Q., Blunt, M. J., & Bijeljic, B. (2012). Modelling two-phase flow in porous media at the pore scale using the volume-of-fluid method. *Journal of Computational Physics*, 231(17), 5653–5668. <https://doi.org/10.1016/j.jcp.2012.04.011>
- Ransohoff, T. C., & Radke, C. J. (1988). Laminar flow of a wetting liquid along the corners of a predominantly gas-occupied noncircular pore. *Journal of Colloid and Interface Science*, 121(2), 392–401. [https://doi.org/10.1016/0021-9797\(88\)90442-0](https://doi.org/10.1016/0021-9797(88)90442-0)
- Shams, M., Raeni, A. Q., Blunt, M. J., & Bijeljic, B. (2018). A study to investigate viscous coupling effects on the hydraulic conductance of fluid layers in two-phase flow at the pore level. *Journal of Colloid and Interface Science*, 522, 299–310. <https://doi.org/10.1016/j.jcis.2018.03.028>
- Singh, K., Bultreys, T., Raeni, A. Q., Shams, M., & Blunt, M. J. (2022). New type of pore-snap-off and displacement correlations in imbibition. *Journal of Colloid and Interface Science*, 609, 384–392. <https://doi.org/10.1016/j.jcis.2021.11.109>
- Singh, K., Menke, H., Andrew, M., Lin, Q., Rau, C., Blunt, M. J., & Bijeljic, B. (2017). Dynamics of snap-off and pore-filling events during two-phase fluid flow in permeable media. *Scientific Reports*, 7(1), 5192. <https://doi.org/10.1038/s41598-017-05204-4>
- Sinton, D. (2014). Energy: The microfluidic Frontier. *Lab on a Chip*, 14(17), 3127–3134. <https://doi.org/10.1039/C4LC00267A>
- Thompson, K. E. (2002). Pore-scale modeling of fluid transport in disordered fibrous materials. *AIChE Journal*, 48(7), 1369–1389. <https://doi.org/10.1002/aic.690480703>
- Wang, Z., Pereira, J.-M., Sauret, E., Aryana, S. A., Shi, Z., & Gan, Y. (2022). A pore-resolved interface tracking algorithm for simulating multiphase flow in arbitrarily structured porous media. *Advances in Water Resources*, 162, 104152. <https://doi.org/10.1016/j.advwatres.2022.104152>
- Xie, C., Lei, W., & Wang, M. (2018). Lattice Boltzmann model for three-phase viscoelastic fluid flow. *Physical Review E*, 97(2), 023312. <https://doi.org/10.1103/PhysRevE.97.023312>

- Xie, C., Raeini, A. Q., Wang, Y., Blunt, M. J., & Wang, M. (2017). An improved pore-network model including viscous coupling effects using direct simulation by the lattice Boltzmann method. *Advances in Water Resources*, *100*, 26–34. <https://doi.org/10.1016/j.advwatres.2016.11.017>
- Zhao, B., MacMinn, C. W., Primkulov, B. K., Chen, Y., Valocchi, A. J., Zhao, J., et al. (2019). Comprehensive comparison of pore-scale models for multiphase flow in porous media. *Proceedings of the National Academy of Sciences*, *116*(28), 13799–13806. <https://doi.org/10.1073/pnas.1901619116>
- Zhao, J., Qin, F., Kang, Q., Qin, C., Derome, D., & Carmeliet, J. (2022). A dynamic pore network model for imbibition simulation considering corner film flow. *Water Resources Research*, *58*(7), e2022WR032332. <https://doi.org/10.1029/2022WR032332>
- Zheng, J., Lei, W., Ju, Y., & Wang, M. (2021). Investigation of spontaneous imbibition behavior in a 3D pore space under reservoir condition by lattice Boltzmann method. *Journal of Geophysical Research: Solid Earth*, *126*(6), e2021JB021987. <https://doi.org/10.1029/2021JB021987>
- Zheng, J., Qi, X., Gong, W., Bian, Y., & Ju, Y. (2024). Investigating snap-off behavior during spontaneous imbibition in 3D pore-throat model by pseudopotential lattice Boltzmann method. *Advances in Water Resources*, *190*, 104751. <https://doi.org/10.1016/j.advwatres.2024.104751>